



HAL
open science

Regolith of the Crater Floor Units, Jezero Crater, Mars: Textures, Composition, and Implications for Provenance

Alicia Vaughan, Michelle E. Minitti, Emily L. Cardarelli, Jeffrey R. Johnson, Linda C. Kah, Paolo Pilleri, Melissa S. Rice, Mark Sephton, Briony H. N. Horgan, Roger C. Wiens, et al.

► To cite this version:

Alicia Vaughan, Michelle E. Minitti, Emily L. Cardarelli, Jeffrey R. Johnson, Linda C. Kah, et al.. Regolith of the Crater Floor Units, Jezero Crater, Mars: Textures, Composition, and Implications for Provenance. *Journal of Geophysical Research. Planets*, 2023, 128, 10.1029/2022JE007437 . insu-04473210

HAL Id: insu-04473210

<https://insu.hal.science/insu-04473210>

Submitted on 23 Feb 2024

HAL is a multi-disciplinary open access archive for the deposit and dissemination of scientific research documents, whether they are published or not. The documents may come from teaching and research institutions in France or abroad, or from public or private research centers.

L'archive ouverte pluridisciplinaire **HAL**, est destinée au dépôt et à la diffusion de documents scientifiques de niveau recherche, publiés ou non, émanant des établissements d'enseignement et de recherche français ou étrangers, des laboratoires publics ou privés.



Distributed under a Creative Commons Attribution - NonCommercial - ShareAlike 4.0 International License

Regolith of the Crater Floor Units, Jezero Crater, Mars: Textures, Composition, and Implications for Provenance



Special Section:

The Mars Perseverance Rover
Jezero Crater Floor Campaign

Key Points:

- Textural, spectroscopic, and chemical analyses of regolith in Jezero crater reveal details of fine, coarse, and mixed grain components
- Compositional information and physical grain characteristics from those analyses inform transport history and possible source material
- Regolith components are compared to their counterparts at other landing sites to inform global versus local inputs to regolith formation

Supporting Information:

Supporting Information may be found in the online version of this article.

Correspondence to:

A. Vaughan,
afvaughan@gmail.com

Citation:

Vaughan, A., Minitti, M. E., Cardarelli, E. L., Johnson, J. R., Kah, L. C., Pilleri, P., et al. (2023). Regolith of the crater floor units, Jezero crater, Mars: Textures, composition, and implications for provenance. *Journal of Geophysical Research: Planets*, 128, e2022JE007437. <https://doi.org/10.1029/2022JE007437>

Received 17 JUN 2022
Accepted 19 JAN 2023

Author Contributions:

Conceptualization: Alicia Vaughan, Michelle E. Minitti, Emily L. Cardarelli

Alicia Vaughan¹ , Michelle E. Minitti² , Emily L. Cardarelli³, Jeffrey R. Johnson⁴ , Linda C. Kah⁵ , Paolo Pilleri⁶ , Melissa S. Rice⁷ , Mark Sephton⁸ , Briony H. N. Horgan⁹ , Roger C. Wiens⁹ , R. Aileen Yingst¹⁰ , Maria-Paz Zorzano Mier¹¹, Ryan Anderson¹² , James F. Bell III¹³ , Adrian J. Brown¹⁴ , Edward A. Cloutis¹⁵ , Agnes Cousin¹⁶ , Kenneth E. Herkenhoff¹² , Elisabeth M. Hausrath¹⁷ , Alexander G. Hayes¹⁸, Kjartan Kinch^{19,20} , Marco Merusi¹⁹ , Chase C. Million²¹ , Robert Sullivan¹⁸ , Sandra M. Siljeström²², and Michael St. Clair²¹ 

¹Apogee Engineering, LLC, Flagstaff, AZ, USA, ²Framework, Silver Spring, MD, USA, ³Jet Propulsion Laboratory, California Institute of Technology, Pasadena, CA, USA, ⁴Johns Hopkins University Applied Physics Laboratory, Laurel, MD, USA, ⁵University of Tennessee, Knoxville, TN, USA, ⁶IRAP, Université de Toulouse, Toulouse, France, ⁷Western Washington University, Bellingham, WA, USA, ⁸Imperial College London, London, UK, ⁹Purdue University, West Lafayette, IN, USA, ¹⁰Planetary Science Institute, Brunswick, ME, USA, ¹¹Centro de Astrobiología (INTA-CSIC), Madrid, Spain, ¹²U.S. Geological Survey, Flagstaff, AZ, USA, ¹³Arizona State University, Tempe, AZ, USA, ¹⁴Plancius Research, Severna Park, MD, USA, ¹⁵University of Winnipeg, Winnipeg, MB, Canada, ¹⁶Institut de Recherche en Astrophysique et Planétologie, Université Paul Sabatier, CNRS, CNES, Toulouse, France, ¹⁷University of Nevada, Las Vegas, Las Vegas, NV, USA, ¹⁸Cornell University, Ithaca, NY, USA, ¹⁹Niels Bohr Institute, University of Copenhagen, Copenhagen, Denmark, ²⁰FOSS Analytics, Copenhagen, Denmark, ²¹Million Concepts, Louisville, KY, USA, ²²RISE Research Institutes of Sweden, Stockholm, Sweden

Abstract A multi-instrument study of the regolith of Jezero crater floor units by the Perseverance rover has identified three types of regolith: fine-grained, coarse-grained, and mixed-type. Mastcam-Z, Wide Angle Topographic Sensor for Operations and eNginEering, and SuperCam Remote Micro Imager were used to characterize the regolith texture, particle size, and roundedness where possible. Mastcam-Z multispectral and SuperCam laser-induced breakdown spectroscopy data were used to constrain the composition of the regolith types. Fine-grained regolith is found surrounding bedrock and boulders, comprising bedforms, and accumulating on top of rocks in erosional depressions. Spectral and chemical data show it is compositionally consistent with pyroxene and a ferric-oxide phase. Coarse-grained regolith consists of 1–2 mm well-sorted gray grains that are found concentrated around the base of boulders and bedrock, and armorings bedforms. Its chemistry and spectra indicate it is olivine-bearing, and its spatial distribution and roundedness indicate it has been transported, likely by saltation-induced creep. Coarse grains share similarities with the olivine grains observed in the *Séítah* formation bedrock, making that unit a possible source for these grains. Mixed-type regolith contains fine- and coarse-grained regolith components and larger rock fragments. The rock fragments are texturally and spectrally similar to bedrock within the *Mááz* and *Séítah* formations, indicating origins by erosion from those units, although they could also be a lag deposit from erosion of an overlying unit. The fine- and coarse-grained types are compared to their counterparts at other landing sites to inform global, regional, and local inputs to regolith formation within Jezero crater. The regolith characterization presented here informs the regolith sampling efforts underway by Perseverance.

Plain Language Summary We used multiple instruments on the Perseverance rover to describe three populations of loose sediments found on the floor of Jezero crater by their grain sizes and chemical compositions. The smallest population has grains that are small sand-sized (80–530 μm) and a mixture of minerals commonly found on Mars, including pyroxene that is present in local rocks and airborne dust found globally. These grains are the easiest to move by wind, so could have distal regional sources as well. Larger gray grains that are 1–2 mm in size and rounded contain olivine. These grains move along the surface, pushed by the impacts of smaller grains that are lifted by the wind. Their size and composition are very similar to olivine grains found in nearby in-place rocks, indicating that they may have a more local source. Finally, there are larger pieces of rocks that have broken down from the erosion of local in-place rocks over time and mix with the other types of grains. Loose sediments within the Jezero crater described here can be compared to loose sediments studied at other landing sites on Mars to help understand how Jezero sediments are formed and transported.

© 2023. The Authors.

This is an open access article under the terms of the [Creative Commons Attribution-NonCommercial-NoDerivs License](https://creativecommons.org/licenses/by/4.0/), which permits use and distribution in any medium, provided the original work is properly cited, the use is non-commercial and no modifications or adaptations are made.

Data curation: Alicia Vaughan, Melissa S. Rice, Briony H. N. Horgan, Roger C. Wiens, Edward A. Cloutis, Agnes Cousin, Alexander G. Hayes, Kjartan Kinch, Marco Merusi, Chase C. Million, Michael St. Clair

Formal analysis: Alicia Vaughan, Michelle E. Miniti, Emily L. Cardarelli, Maria-Paz Zorzano Mier, Kenneth E. Herkenhoff

Funding acquisition: James F. Bell, Kenneth E. Herkenhoff

Investigation: Alicia Vaughan, Michelle E. Miniti, Emily L. Cardarelli, Briony H. N. Horgan, Elisabeth M. Hausrath, Chase C. Million, Robert Sullivan, Sandra M. Siljeström

Methodology: Alicia Vaughan, Michelle E. Miniti, Emily L. Cardarelli, Jeffrey R. Johnson, Linda C. Kah, Melissa S. Rice, R. Aileen Yingst

Resources: James F. Bell

Software: Melissa S. Rice, Chase C. Million, Michael St. Clair

Supervision: James F. Bell

Validation: Alexander G. Hayes, Kjartan Kinch, Marco Merusi

Visualization: Paolo Pilleri, Chase C. Million, Michael St. Clair

Writing – original draft: Alicia Vaughan, Michelle E. Miniti, Emily L. Cardarelli, Mark Sephton, Maria-Paz Zorzano Mier

Writing – review & editing: Jeffrey R. Johnson, Linda C. Kah, Melissa S. Rice, Briony H. N. Horgan, Roger C. Wiens, R. Aileen Yingst, Ryan Anderson, Adrian J. Brown, Edward A. Cloutis, Agnes Cousin, Kenneth E. Herkenhoff, Robert Sullivan

1. Introduction

The Perseverance rover landed in Jezero crater, Mars on 18 February 2021 at the “Octavia E. Butler” landing site, beginning its mission to sample an ancient crater lake basin seeking signs of ancient microbial life. After rover commissioning activities (~100 sols), Perseverance began the Crater Floor Campaign (Sun et al., 2022). The focus of the Crater Floor Campaign was to explore and sample the crater floor units southeast of the Jezero delta. The photogeologic map produced by the Mars 2020 science team of the Perseverance field site within Jezero crater (Stack et al., 2020) defined bedrock units within the crater floor: crater-floor-fractured-1 (*Cf-f-1*), crater-floor-fractured-2 (*Cf-f-2*), and crater-floor-fractured-rough (*Cf-fr*), which are variably overlain by an undifferentiated smooth unit (*Us*) and aeolian bedforms (*Ab-l* and *Ab-s*). Studies of Jezero prior to its selection as the Mars 2020 landing site identified the *Cf-f-1* and *Cf-f-2* units as the oldest exposed deposit within the crater floor, underlying *Cf-fr* (Goudge et al., 2015, 2017). The *Cf-f-1* and *Cf-f-2* units are equivalent to the light-toned floor unit of Goudge et al. (2015), and exhibit olivine and carbonate signatures of varying relative strengths throughout their exposures (e.g., Brown et al., 2020; B. L. Ehlmann et al., 2008; Goudge et al., 2015; B. H. N. Horgan et al., 2020; Murchie et al., 2007; Mustard et al., 2009). The presence of olivine supported a variety of origin hypotheses (Goudge et al., 2015; V. E. Hamilton & Christensen, 2005; Hoefen et al., 2003; Kremer et al., 2019; Mustard et al., 2009) including intrusion, impact melt sheet, lava flows, airfall tephra or lacustrine deposit. The presence of carbonate was interpreted as an alteration of the olivine (e.g., B. L. Ehlmann et al., 2008; Goudge et al., 2015; Viviano et al., 2013). *Cf-fr* was hypothesized as a volcanic unit based on its visible and near-infrared (NIR) (400–2,500 nm) and thermal infrared spectral signatures (e.g., signatures of pyroxene and/or olivine; Goudge et al., 2012, 2015; B. H. N. Horgan et al., 2020; Salvatore et al., 2018), degree of crater retention (Goudge et al., 2015; Schon et al., 2012), lobate margins, and apparent embayment relationships with the delta and *Cf-f-1* and *Cf-f-2* terrains (Goudge et al., 2012, 2015; Ruff, 2017; Schon et al., 2012). However, a sedimentary origin of *Cf-fr* could not be ruled out from the orbit based on these properties alone, so alternative pyroclastic and sedimentary origins were also suggested (B. H. N. Horgan et al., 2020; Stack et al., 2020). Given its smooth texture from orbit, lower thermal inertia relative to *Cf-fr* and *Cf-f-1*, and stratigraphic position over bedrock, possible origins ascribed to the *Us* unit included tephra, aeolian deposits, or a lag deposit of sediments from the breakdown of rocks and erosion of the landscape (Ferguson et al., 2006; Stack et al., 2020). The Crater Floor Campaign traverse of the Perseverance rover crossed the *Cf-fr*, *Cf-f-1*, and *Us* units.

The in situ observations of lithology, stratigraphy, chemistry, and mineralogy made by the Perseverance payload during the Crater Floor Campaign (Sun et al., 2022) redefined these orbital units. *Cf-f-1* is identified as the *Séítah* formation and *Cf-fr* is identified as the *Mááz* formation. The *Séítah* formation is interpreted as an olivine cumulate carbonated under low water/rock ratio conditions, and the *Mááz* formation as a series of basaltic lava flows or fractionation complement to the olivine cumulate (Farley et al., 2022; Liu et al., 2022; Scheller et al., 2022; Wiens et al., 2022).

Regolith on Mars has been previously defined as unconsolidated particulate material generated by weathering of bedrock and the addition of wind-blown material and airfall dust (Arvidson et al., 1989, 2017; Moore et al., 1987; Yen et al., 2005). Regolith covered much of the Crater Floor Campaign traverse represented by the *Us* unit, and was present in close association with both *Mááz* and *Séítah* bedrock. Aeolian bedforms from individual decimeter-to meter-scale ripples to dune fields were also encountered throughout the Campaign. Scientific goals of the Crater Floor Campaign included the characterization of the regolith and aeolian bedforms, and investigation of weathering, erosion, and transport of loose sediments within Jezero. Insights gained through these investigations support comparisons to regolith at other landing sites to better understand the role of local and global mixing in the formation of regolith across the planet. This is particularly critical to helping the Mars 2020 Science Team prioritize regolith target “types” for future regolith sample collection. For example, how should a Jezero regolith sample prioritize collection of a global dust component compared to perhaps a more local component present in coarser material? Previous missions have shown similarities among regolith across landing sites, particularly in the dust component and the finest fraction (Clark et al., 1982; Gellert et al., 2004; O’Connell-Cooper et al., 2017, 2018; Yen et al., 2005; Sullivan et al., 2008). Similarities observed in the fine-grained regolith of Jezero indicate that such a sample could provide a globally relevant perspective on the composition of Martian fine-grained regolith and provide further insight into its formation and possible transport scales. To further evaluate the extent and influence of local mixing in the regolith formation, returned regolith samples from Jezero can be directly compared to the returned local rock sample cores. Thus, regolith samples have high scientific value that will help constrain our understanding of weathering and sediment transport on Mars. Here, we present a

coordinated, multi-instrument investigation (Mastcam-Z, SuperCam, and Wide Angle Topographic Sensor for Operations and eNginneering [WATSON]) that provides cross-scale characterization of the textural, geochemical, and spectral properties of the regolith encountered during the Crater Floor Campaign in Jezero crater.

2. Area of Regolith Analysis

Regolith observations were acquired at *Octavia E. Butler* landing site during rover commissioning, helicopter operations, and initial exploration of the crater floor, and during the Crater Floor Campaign that followed thereafter. The Crater Floor Campaign continued until Sol 380, but the regolith observations of this study end at Sol 350, near the southwestern extent of the *Séítah* region visited by the rover. After this part of the Crater Floor Campaign, Perseverance rapidly retraced its path northward through the Campaign area back to and beyond the landing site. As such, Sol 350 (February 2022) makes a natural cut off point to focus on the study. Over this time, 47 regolith-focused or rock-regolith interface targets were acquired with varying combinations of instruments (Table 1, Figure S1, Table S1 in Supporting Information S1).

3. Instrumentation and Methods

Our study utilized data products from three instruments onboard the rover and applied analytical techniques incorporating images, multispectral observations, and chemical studies. Color, texture, grain size, and rounding of grains within regolith targets were assessed using images from Mastcam-Z (Bell et al., 2021), hand-lens quality images from the arm-mounted WATSON (Bhartia et al., 2021), and images from the SuperCam Remote Micro Imager (RMI; S. Maurice et al., 2021). Visible through NIR (442–1,022 nm) spectral capabilities of Mastcam-Z helped to constrain iron mineralogy in regolith targets. Regolith elemental chemistry was determined using the laser-induced breakdown spectroscopy (LIBS) capability of SuperCam (Wiens et al., 2021).

3.1. Instrumentation

3.1.1. Mastcam-Z

Mastcam-Z (Bell et al., 2021; Hayes et al., 2021) acquires images through a pair of zoomable stereoscopic cameras mounted on a Remote Sensing Mast 2.1 m above the surface. Each camera has a Bayer-pattern red, green, and blue (RGB) array (Bayer, 1976) on the charge-coupled device (CCD) and a filter wheel that enables multispectral imaging in 14 narrowband visible to NIR wavelengths between the two cameras (442–1,022 nm). All Mastcam-Z images shown in this work are left-eye (L0; IR cutoff filter for visible imaging) enhanced color images. Enhanced color images are debayered to create RGB channels; pixels in those channels are clipped at 1.25 and 99th percentiles, and those pixel values are normalized to a full 0–255 stretch. The longest focal length of 110 mm enables the resolution of ~500 μm grains at 2 m (Bell et al., 2021). Grain size measurements for this study were obtained from 110 mm focal length images of targets 2.24–3.0 m from the rover, resolved at 150–210 $\mu\text{m}/\text{pixel}$ (Tables 1 and 2). Mastcam-Z data were calibrated following the process detailed in Hayes et al. (2021), which removes instrument noise, performs geometric calibration, and converts digital numbers to radiance values. For multispectral analyses, calibrated radiance data were then converted to reflectance values (IOF) using coefficients from measurements of the rover calibration target obtained nearly contemporaneously. Mastcam-Z spectral data are shown in units of reflectance factor (R^*), which is the IOF value divided by the cosine of the solar incidence angle ($\text{IOF}/\cos(i)$). The right eye is scaled to the left eye at 800 nm, and the spectra are averaged at overlapping wavelengths between the left and right eye filters. Variance bars indicate the standard deviation of reflectance values from those pixels on each filter's associated image that fall within the specific region of interest (ROI). Details about the Mastcam-Z onboard calibration targets and their use in generating reflectance factor data can be found in Kinch et al. (2020) and Merusi et al. (2022). Additional details about the software tools developed for multispectral data processing tasks can be found in Million et al. (2022).

3.1.2. WATSON

The WATSON camera is part of the Scanning Habitable Environments with Raman and Luminescence for Organics and Chemicals (SHERLOC) investigation (Bhartia et al., 2021). SHERLOC and WATSON are located together on the turret at the end of the Perseverance robotic arm (Moeller et al., 2021). WATSON, similar to its precursor, the Mars Science Laboratory Mars Hand Lens Imager (Edgett et al., 2012, 2015), yields color via a Bayer pattern filter over a $1,640 \times 1,214$ pixel CCD ($1,600 \times 1,200$ photoactive pixels), and utilizes a focus

Table 1
Regolith Targets^a

Sol	Target	Mastcam-Z MS ^b	SuperCam	WATSON	Unit	Target type ^c
70/71	Tsewozitah (tsé'éwózítah)	x	x	x	Máaz	Coarse
72	A koo (ak'óó)	x	x		Máaz	Coarse
84	Sei (séí)	x	x		Máaz	Fine
84	Naakih (naaki)	x	x		Máaz	Mixed
103	As dzoh (asdzoh)	x	x		Máaz	Mixed
103	Niyol (níyol)	x			Máaz	Fine, coarse
104	Sey dey yilki (séí bił yílk'id)	x	x		Máaz	Coarse
106	Alk ee aznil (alkéé'aznil)	x		x	Máaz	Coarse, mixed
106	(Hastaa) hastáá	x	x		Máaz	Coarse
110	Lha tsadah (há'ts'áadah)	x	x		Máaz	Coarse
115	Queh eh (kwe'é)		x	x	Máaz	Mixed
123	Whoosh (hosh)	x	x		Máaz	Fine
130	Raton	x			Máaz	Fine, coarse
134	Pierrefeu	x			Máaz	Coarse
137	Roque		x		Máaz	Coarse
138/144	Foux	x	x	x	Máaz	Fine, coarse
150	Clave	x	x		Máaz	Coarse
185	Chambares	x	x		Máaz	Coarse
191	Digne les Bains	x			Máaz	Fine, coarse
203	Rourebel	x			Séítah	Mixed
208	Auvere	x			Séítah	Mixed
250	Pont du Loup	x		x	Séítah	Coarse
254	Ferres	x			Séítah	Mixed
257	Salette			x	Séítah	Fine
282	Rougon		x		Séítah	Coarse
282	Norante	x			Séítah	Fine
286	Demandoix	x			Séítah	Mixed
291	Calern	x	x		Séítah	Fine
293	Pauls	x		x	Séítah	Fine
302	Brandis	x	x		Séítah	Mixed
308	Seítah Artuby contact	x			Séítah	Mixed
312	Ripert	Z110			Séítah	Coarse
313	Tanaron	x	x		Séítah	Fine, coarse
315	Chandon	x	x		Séítah	Coarse
324	Amen + Callas	Z110	x		Séítah	Coarse
333	Toudon	x	x		Séítah	Fine, mixed
335	Rigelet	x			Séítah	Mixed

^aTargets for which individual spectra, chemistry and/or grain size are featured within figures; additional regolith targets that contributed to average spectra are listed in Table S2 in Supporting Information S1. ^bx denotes which technique was employed at a given target. For Mastcam-Z, "Z110" notes targets where only red, green, and blue images were taken and multispectral data was not acquired. ^cType denotes the primary regolith type(s) targeted within the image.

mechanism to produce in-focus images from 1.78 cm working distance to infinity (Bhartia et al., 2021; Edgett et al., 2015). For targets whose topography exceeds the depth of field at a particular working distance, a focus stack of images (typically 8) is acquired, and the best focus portions of those images are combined on board to create a focus merge product and range maps for the target. The focus capability of WATSON and position on the

Table 2
Instrument Resolutions

Instrument	Pixel scale ^a	Minimum grain size resolved
Mastcam-Z (110 mm focal length) ^b	150–210 $\mu\text{m}/\text{pixel}$ @ 2.24–3 m target distances	~500 μm
WATSON	20–135 $\mu\text{m}/\text{pixel}$ @ 4–35 cm target distances	60 μm
SuperCam RMI	20–40 $\mu\text{m}/\text{pixel}$ @ 2.2–4.1 m target distances	160 μm

^aReported for target distances utilized in this study. ^bOnly measured coarse grains.

robotic arm permit WATSON to support Perseverance by acquiring images over a range of working distances. WATSON images support characterization of regolith target color, grain size, grain size distribution, rounding, and texture, achieving pixel scales at closest approach (13.1 $\mu\text{m}/\text{pixel}$ at 1.78 cm working distance) capable of resolving silt-size grains (e.g., Wentworth, 1922). The complexity and resources associated with robotic arm deployment and placement limit the use of WATSON; thus, WATSON regolith observations in this study were largely obtained at sites when the rover was stationary for several sols for either focused helicopter operations, robotic arm qualification activities, or sampling (Table 1).

3.1.3. SuperCam

SuperCam is a multifunctional remote-sensing instrument capable of investigating the mineralogy and elemental composition of targets using a color imager, the RMI, a microphone, and laser and passive spectroscopy activities including visible and infrared (VISIR) spectroscopy (~400–2,600 nm), LIBS, and Raman spectroscopy (S. Maurice et al., 2021; Wiens et al., 2021). We used imaging (RMI) and LIBS results from SuperCam, which were collected through a co-boresighted unit atop the rover mast (S. Maurice et al., 2021; Wiens et al., 2021). During the Crater Floor Campaign, SuperCam near- and mid-field observations incorporating regolith were acquired from targets 2.2–15 m from the rover. RMI imaging yields high resolution color context for LIBS and spectroscopy measurements, and standalone images of targets for grain to landscape scale texture and structure (e.g., Mangold et al., 2021). RMI resolution is $\leq 80 \mu\text{rad}$ (defined as a line pair with more than 20% contrast), allowing 160 μm grains to be resolved at 2 m distance from the instrument (S. Maurice et al., 2021; Table 2). LIBS data were acquired using a laser emitting at 1,064 nm with a focused beam diameter of 350 μm utilized to collect 5–10 point rasters for each target, covering up to 18.8 mrad (Wiens et al., 2021). The LIBS data used here includes the target's elemental abundances as eight major rock-forming oxides from a footprint of 0.25–0.45 mm (Anderson et al., 2022).

3.2. Methods

3.2.1. Measurements of Grain Size, Roundedness, Statistical Analyses, and Data Visualization

Regolith grain characteristics for 20 targets were assessed using Mastcam-Z, WATSON, and RMI images. The choice of grains to analyze in each image was made based primarily on image resolution, which is a function of distance to target (Table 2). Distance to a given target is relatively consistent for WATSON images, as a relatively narrow range of standoff distances is commonly used, but distance can vary significantly for Mastcam-Z and RMI images as Mastcam-Z in particular is designed to image out to infinity. To ensure the consistency of scale, only grains within a limited distance range were analyzed. For Mastcam-Z, grain size measurements were obtained from images acquired 2.24–3 m from the camera, yielding pixel scales of 150–210 $\mu\text{m}/\text{pixel}$ (Table S1 in Supporting Information S1). For SuperCam RMI, grain size and rounding observations of this study were limited to images obtained from 2.2 to 4.1 m from the instrument, permitting the resolution of grains from ~175 to 330 μm (Table S1 in Supporting Information S1). For WATSON, measurements of coarse (>500 μm) grains and evaluation of their roundedness were conducted in images obtained from working distances of 15–35 cm, yielding pixel scales of 60–135 $\mu\text{m}/\text{pixel}$. Measurement of finer grained components (<500 μm) were limited to WATSON images with pixel scales of 20–23 $\mu\text{m}/\text{pixel}$, and a single RMI mosaic (target “Foux”; Table 1) that was acquired from a target distance (2.28 m) and resolved ~175 μm grains. At least three pixels across the long axis of a grain are required to confidently identify a grain and assess size, while to assess other characteristics such as roundedness requires additional pixels so that the shape of grain corners, edges and surfaces can be determined. For this study, we conservatively chose a limit of >3 pixels long axis to assess size; for roundedness, we chose

>9 pixels for WATSON images, and >20 pixels for RMI images. Grains below these limits were not assessed. In addition to these resolution constraints, we analyzed only those grains that were in the clear focus, and in either full sun or full shadow illumination to aid the consistency of grain size measurements across each image.

Using these limits, 3,314 grains were assessed for size; a subset of these grains ($n = 401$) in 10 regolith targets in the *Máaz* and *Séítah* formations were assessed for roundedness. As a proxy for size (B. E. Ehlmann et al., 2017; Herkenhoff et al., 2004; Weitz et al., 2006, 2018), the length of the longest axis of individual grains was manually measured using the Affinity Photo and ImageJ (<https://imagej.nih.gov/ij/index.html>) software environments. Grain roundedness was qualitatively assessed relative to standards defined in Powers (1953) for very angular to well-rounded grains. This technique has been employed in other studies of grains and clasts on Mars (e.g., Khan et al., 2022; Yingst et al., 2008; Yingst et al., 2016). Roundedness evaluation was limited to WATSON and RMI images and mosaics because Mastcam-Z images lacked sufficient resolution to confidently assess rounding.

To evaluate relationships and trends in grain size and rounding across the targets, several statistical tests were conducted and visualized in the R software environment (version 4.1.1; R Core Team, 2021). All statistical visualizations were completed by employing the ggplot and ggpubr packages with their respective dependencies. Sample-based and image-based grain size distributions and the grain size averages were calculated using ggplot and the geom_boxplot() settings. The application of a Shapiro-Wilks test determined the non-normality of the distribution of grain size measurements and nonparametric analyses were completed, including a Wilcoxon rank-sum test to conduct geologic unit-based comparisons or specific roundedness comparisons as well as Kruskal-Wallis tests to examine lithologic-based comparisons (i.e., multiple groups). For all statistical tests completed, if the output p-values were less than 0.05 then the value indicates with greater than 95% confidence that the comparison was not due to random sampling from the same distribution, and is therefore statistically significant.

3.2.2. Regolith Spectroscopy

Mastcam-Z multispectral analysis helps constrain the regolith iron mineralogy and is supported by a subset of SuperCam LIBS measurements. For Mastcam-Z, spectra were averaged from ROIs covering representative regolith targets within the IOF calibrated images for each multispectral observation (Rice et al., 2023). We used software tools developed for analyzing Mastcam-Z multispectral data (Million et al., 2022; St. Clair et al., 2022) that enabled relatively quick assessment of images based on a standard set of multispectral products and capture relevant metadata about every spectrum collected for inclusion in a large spectral database. For regolith ROIs, we assigned a relative grain size (coarse, fine, and mixed) and location (bedform, on rock, undisturbed surface, disturbed surface, on hardware, etc.). Spectra within the assembled database were evaluated using spectral parameters (e.g., band ratios, band depths) and filtered by using associated metadata (e.g., magnitude of standard deviation, time of sol).

Average spectra were calculated from regolith ROIs through Sol 350 for targets within both the *Máaz* and *Séítah* formations. Examples of these ROIs are shown in Figure 1. Table S2 in Supporting Information S1 includes all sequences used in these averages. The nearfield targets included in these averages were within a few meters of the rover to support accurate textural classification. Error bars in the spectra indicate the standard deviation of reflectance values from those pixels on each filter's associated image that fall within the specific ROI. This is actually variance, not error, and tends to be much larger than actual instrumental error. All Mastcam-Z team-collected ROI context images and spectra through the Crater Floor campaign have been archived by Rice et al. (2023).

3.2.3. Regolith Chemistry

The SuperCam LIBS elemental composition of the regolith types presented are derived from targets throughout the study area (Table 1, Table S1 in Supporting Information S1). For each raster spot, 25–45 laser shots were collected after dust-clearing the area of interest via the first five laser shots. The elemental abundances for each given raster spot are averages of the non-dust shots, and are reported as eight major-element oxides (SiO_2 , TiO_2 , Al_2O_3 , FeO_T , MgO , CaO , Na_2O , and K_2O , where FeO_T indicates that all iron is quantified in the +2 state) (Anderson et al., 2022). The laser ablation process in LIBS breaks apart most molecules, and thus the technique detects primarily atomic emission lines. However, the regression methods used for LIBS quantification are based on laboratory measurements of geostandards for which the certified composition is reported as oxides, and many standard geochemical plots are also calculated based on oxide abundance. Therefore, SuperCam major element quantification is also reported in terms of oxides. For elements with multiple oxidation states such as Fe, it is simpler to report the composition in terms of a single oxidation state. This should not be interpreted as



Figure 1. Mastcam-Z regolith types overview. All images are L0 (Bayer) enhanced color that provides an overview and context for the different regolith types identified [fine-grained regolith (F), coarsest gray grains (C), and mixed-type (M)]. Colored boxes represent regions of interest for the coarse (blue) and fine (red) grained regolith for the average spectra shown in Figure 8. Unless otherwise specified, images were acquired at 110 mm focal length. (a) *Demandoux* (Sol 286, zcam03265, 63 mm focal length), (b) *Niyol* (Sol 103, zcam03150, 79 mm focal length), and (c) *Lha tsaadah* (Sol 110, zcam03160, 34 mm focal length) exhibit the coarse, fine-grained, and mixed types of regolith. (d) *Sey dey yilkid* (Sol 104, zcam3151, 63 mm focal length) and (e) *Hastaa* (Sol 106, zcam03153) contain bedforms armored by coarse gray grains surrounded by mixed type regolith. Panels (d) and (e) were taken from the same rover location, with panel (e) providing a higher spatial resolution of the same type of bedform. (f) *Pierrefeu* (Sol 134, zcam03177), (g) *Foux* (Sol 138, zcam03181), and (h) *A koo* (Sol 72, zcam03123) show coarse grained regolith surrounding *Máaz* paver rocks. (i) *Naakih* (Sol 84, zcam03133) shows a representative mixed type regolith surface. (j) *Whoosh* (Sol 123, zcam03168), (k) *Raton* (Sol 130, zcam03175), and (l) *Toudon* (Sol 333, zcam03304) show disturbed regolith in various settings. SuperCam LIBS pits are present in panels (h, j, l).

an assertion that all of the iron is in that state; it simply reflects a lack of information about the oxidation state and a desire to avoid making an assumption about the ratio of $\text{Fe}^{2+}/\text{Fe}^{3+}$. As detailed by Anderson et al. (2022), the accuracy of LIBS reported weight percentages for these major element oxides was determined by the root mean square error of prediction for a test set of data, and are as follows: $\text{SiO}_2 = 6.1\%$, $\text{TiO}_2 = 0.3\%$, $\text{Al}_2\text{O}_3 = 1.8\%$, $\text{FeOT} = 3.1\%$, $\text{MgO} = 1.1\%$, $\text{CaO} = 1.3\%$, $\text{Na}_2\text{O} = 0.5\%$, and $\text{K}_2\text{O} = 0.6\%$. SuperCam LIBS data has been shown to be more precise than it is accurate, making it particularly useful in observing changing trends in composition (Anderson et al., 2022). To assess the lithologic and geologic unit-based variability within spot-to-spot LIBS raster data, ternary diagrams based on molar abundances were generated using the ggtern package (N. E. Hamilton & Ferry, 2018) within the R software environment (version 4.1.1; R Core Team, 2021). Each LIBS spot is colored by the target and labeled by raster number, allowing each raster spot of a target to be visualized in a ternary diagram for comparison of their chemical compositions relative to other targets as well as standards.

4. Results

We identified three types of regolith in the Jezero crater floor units: fine-grained, coarse-grained, and mixed type (Figures 1–4). These three components occurred throughout the rover traverse of both the *Máaz* and *Séítah* formations.

4.1. Regolith Components and Textural Properties

Fine-grained regolith is found surrounding bedrock slabs and boulders, comprising bedforms, and collected on top of rocks in erosional depressions (Figure 1). It is widespread and commonly intermixed with coarse-grained regolith, either underlying or acting as matrix material for coarser-grained material. It also appears on surfaces disturbed by the rover activity, such as in wheel tracks, where the coarser grains were pushed under the surface and into the fine-grained component, and underlying or surrounding rocks dislodged by rover mobility (Figures 1k and 11). Fine-grained regolith characterized by WATSON and SuperCam RMI includes grains with long axes between ~ 80 and $530 \mu\text{m}$ (very fine to medium sand; Wentworth, 1922) (Figure 2a, Figure S5b in Supporting Information S1). Relative color variations in uncalibrated WATSON and RMI images suggest that fine-grained regolith comprises red, black, variably gray, white, and translucent grains, indicating a mixture of minerals. Airfall dust, visible as reddened surfaces and/or resulting from clumping that leads to resolvable composite particles, is also intimately mixed with the grains. These characteristics are observed in fine-grained regolith whether the regolith occurs within *Máaz* or *Séítah* formations. Fine-grained regolith contains the grain sizes most easily transported by saltation on Mars (100 – $150 \mu\text{m}$) (Greeley et al., 1980; Iversen & White, 1982; Swann et al., 2020), and, accordingly, a wind event between Sols 313 and 317 (Lemmon et al., 2022a, 2022b) deposited fine-grained particles onto the rover deck (Figure 3).

Coarse-grained regolith, predominantly comprised of well-sorted gray grains, is observed in several settings, including concentrated around the base of boulders and bedrock, on top of bedrock slabs, scattered around and included in the undisturbed surface of a mixed type of regolith, and armoring bedforms whose interiors are dominated by fine-grained regolith (Figures 1, 2b, 2c and 4a). The intimate association of fine and coarse-grained regolith types occurs in all coarse-grained type settings (e.g., Figures 2 and 4). The average long axis of the coarse gray grains within an individual target was measured to be between 1.01 and 1.88 mm (Figure 5), that is, very coarse sand (Wentworth, 1922). Each individual target, however, exhibits a range of grain sizes, from coarse sand (0.5 – 0.7 mm) to granule size (2 – 2.6 mm), with a small number (<10 grains) of outliers of very fine pebble size (3 – 4 mm). With the exception of the outlier grains, the range of grain sizes of *Máaz* targets and *Séítah* targets is the same. In targets where coarse regolith grains were measured in more than one image type (Table 1, Figure 5), differences among average long axis measurements ranged from 50 to $250 \mu\text{m}$. These differences do not alter the findings of the collective data set, as the ranges of individual grain sizes and average grain sizes derived from an individual instrument have the same pattern as the collective data set (Figure S2 in Supporting Information S1). The full range of average grain sizes is present in targets within both *Máaz* and *Séítah* (Figure 6). The dominant average grain sizes fall between 1.0 and 1.6 mm , with targets of this average size at every site along the traverse. The only instances of targets with average grain sizes $>1.6 \text{ mm}$ were found along the southern part of the traverse, near and within *Séítah*. The pattern of larger average grain sizes along this part of the traverse persists even when measurements are limited to those from a single instrument (Figure S3 in Supporting Information S1). The degree of rounding of coarse grains ranged from subangular to be well rounded (Powers, 1953), with the majority of grains in each target falling within the subrounded and rounded categories (Figure 7). The predominance of subrounded to rounded grains is observed

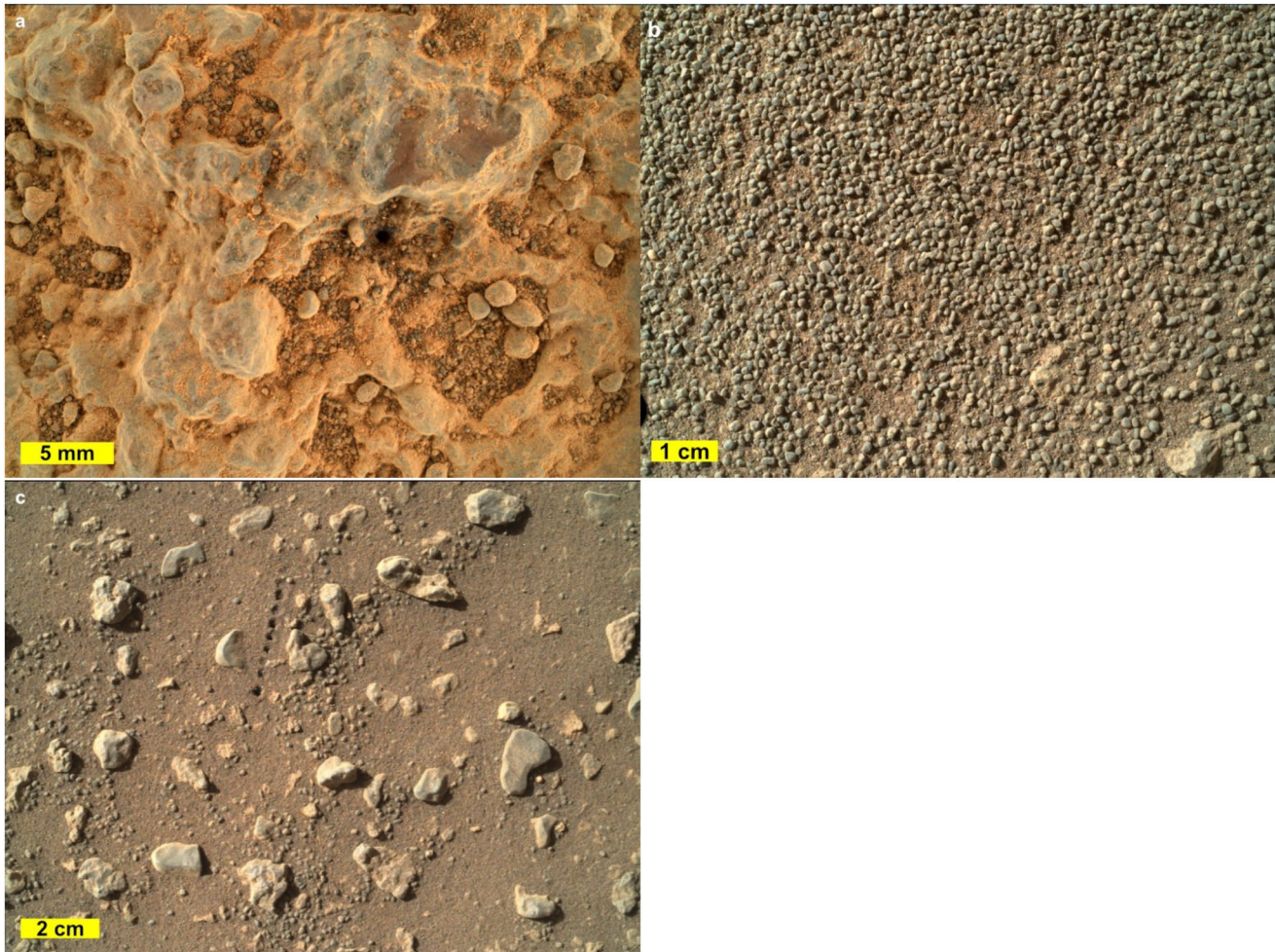


Figure 2. Wide Angle Topographic Sensor for Operations and eNginering images of regolith types. (a) Fine-grained red regolith present in bedrock depressions in target *Foux*. The focus merge product acquired from 4 cm working distance, Sol 140 (S11_0140_0679334136_035ECZ_N0051812SRCL00003). (b) Coarse gray grains present on the flank of a small ripple, target *Alk ee aznil*. Focus merge product acquired from 15 cm working distance, Sol 106 (S11_0106_0676364404_070EZZ_N0040592SRCL000053). (c) Mixed regolith present with the *Máaz* formation, target *Queh eh*. Full frame image acquired from 25 cm working distance, Sol 115 (SIF_0115_0677161052_339EBY_N0041062SRCL02503).

whether considering measurements from the collective rounding data set (Figure 7) or individual instruments (Figure S4 in Supporting Information S1).

The mixed-type regolith is characterized by a poorly sorted mixture of materials that includes the fine-grained regolith as a matrix or underlying material, scattered coarse gray grains, and angular rock fragments of ~2–20 mm in longest dimension (very fine to coarse pebbles; Wentworth, 1922) (Figures 1, 2c and 4b). The smaller population of rock fragments grades into grain sizes that comprise the coarse-grained regolith (e.g., Figures 2c and 4b). Rock fragments of the mixed-type regolith typically share color and texture with local bedrock neighboring occurrences of the mixed-type regolith. Mixed-type regolith comprises much of the *Us* unit (Stack et al., 2020) surface traversed by the rover during the Crater Floor Campaign, with the exception of regions that are covered in aeolian bedforms. It is also prevalent around individual rocks and larger bedrock exposures throughout the campaign area.

4.2. Regolith Spectroscopy and Chemical Composition

4.2.1. Mastcam-Z Multispectral Data

Average Mastcam-Z spectra for fine- and coarse-grained regolith are shown alongside the average Jezero dust spectrum in Figure 8. The dust spectrum is an average of all regions classified as “thick dust” in the spectral data-

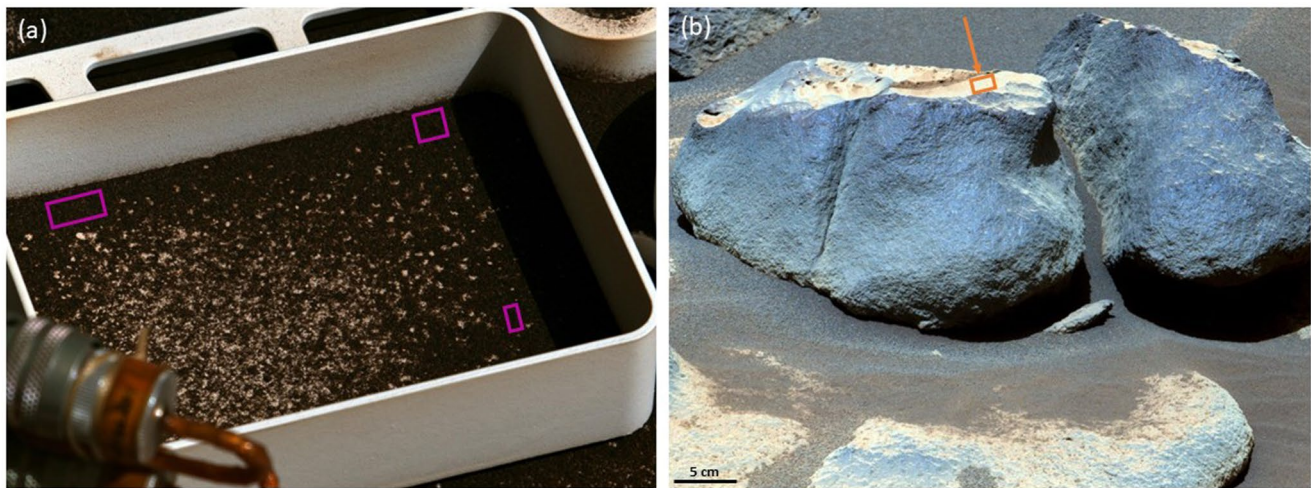


Figure 3. (a) Sol 344 (zcam03312) rover deck image showing fine-grained regolith collected on the rover deck after a regional dust storm between Sols 313 and 317. The receptacle is 10 cm across. The magenta boxes are the regions of interest (ROI) used to collect the average spectrum of this material shown in Figure 8. (b) Sol 86 (zcam03135) rock target *Yani* showing an example of an ROI classified as “thick dust” collected from a rock surface. ROIs such as this one were exported from our spectral database and averaged to produce the Jezero dust spectrum shown in Figure 8.

base, and a representative example is shown in Figure 4. Care was taken to ensure that ROIs classified as “thick dust” were dust covered such that the underlying rock is not visible, which can be easily assessed by comparison to cleaner portions of the rocks in the same image. As such, it is possible that these ROIs are not strictly airfall dust, but could include at least some minor component of the underlying material as well. A spectrum for the fine-grained regolith deposited on the rover deck after the Sol 313–317 dust storm is also included. This spectrum represents recently mobilized fine-grained regolith that is assumed to be relatively dust free. Imaging shows these grains to be relatively dark, and much less red than undisturbed fine-grained regolith on the surface that has had more time to accumulate airfall dust (Figure 3). The overall shape of the spectrum is similar to the average fine-grained regolith spectrum, but darker with a weaker red slope consistent with this material being less dusty. Fine-grained regolith exhibits a peak reflectance at 754 nm, a broad NIR absorption centered between 910 and 978 nm, and ferric absorption at 528. The fine-grained regolith is redder in color than the coarse-grained regolith, with a red/blue ratio (R^*_{754}/R^*_{442}) that is 25% higher than that of coarse-grained regolith. The coarse-grained regolith exhibits a shorter peak reflectance at 677 nm followed by flat to negative NIR slopes from 866 to 1,022 nm (Figure 8). Fine- and coarse-grained regolith are easily distinguishable from the average dust spectrum, which is much brighter, with a steeper red edge, and a narrow absorption feature at 866 nm.

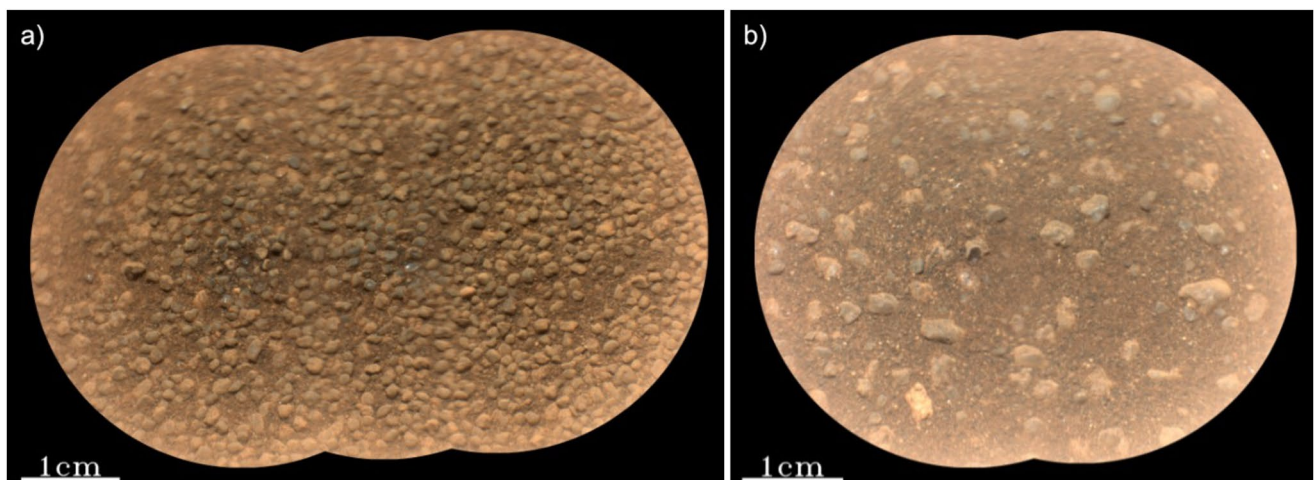


Figure 4. SuperCam Remote Micro Imager mosaics of regolith targets. (a) Coarse-grained regolith on fine grained regolith, target A koo (Sol 72). The same target is also pictured in Figure 1h. (b) Mixed regolith at target Naahik (Sol 84). The same target is also pictured in Figure 1i.

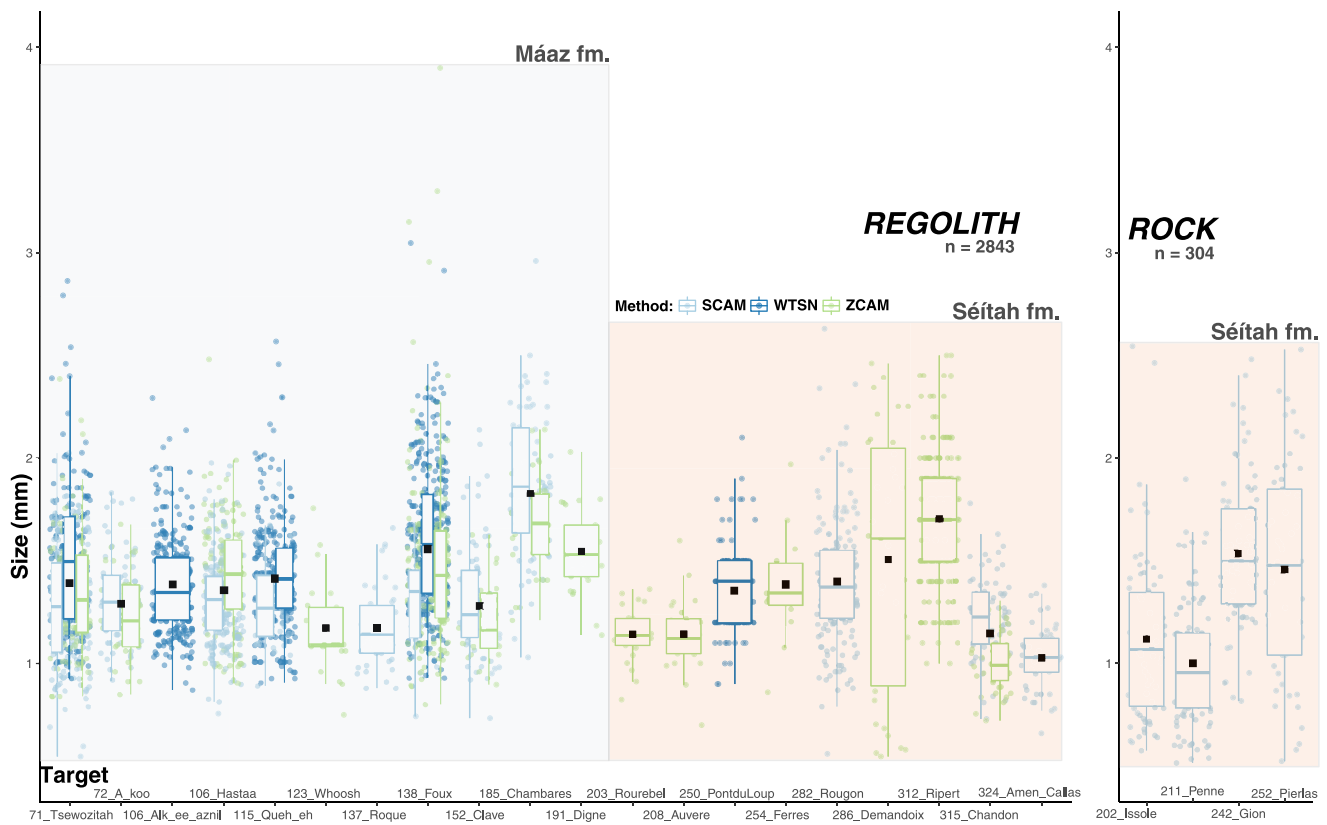


Figure 5. Sample-based boxplots of coarse-grained regolith grain sizes measured in regolith (left panel) using Mastcam-Z, SuperCam Remote Micro Imager, and Wide Angle Topographic Sensor for Operations and eNgeering (WATSON) images and colored by image type (light blue—SuperCam, dark blue—WATSON, green—Mastcam-Z), with the respective geologic units represented as shaded boxes (blue—*Máaz*, orange—*Séítah*). The regolith grain sizes observed in the *Máaz* and *Séítah* formations are compared to grain sizes measured within *Séítah* formation rocks (right panel). Average grain size is denoted by the black dots. The “boxes” represent where the data’s 25th percentile (bottom of box), 50th percentile (center line of the box, median of the data), and the 75th percentile (top of the box) fall. The lines extending from the boxes go toward the minimum or maximum values found within the data set, thereby showing the range as well as the distribution of the data. The regolith targets are arranged by sol (increasing along the x-axis), which serves as a rough proxy for position along the traverse (moving south along the x-axis).

Mixed regolith is a mixture of fine- and coarse-grained components, and granule- to pebble-sized rock fragments. As such, we expect the spectral signature of a mixed regolith ROI to incorporate features associated with both fine- and coarse-grained regoliths and rock fragments. With fine- and coarse-grained regolith components characterized by averages in Figure 8, we collected spectra from rock fragments in mixed regolith from both the *Máaz* and *Séítah* formations to complete characterization of mixed regolith components. Figure 9 shows the spectra of specific rock fragments from example-mixed regolith surfaces compared to nearby in-place rocks in the *Máaz* and *Séítah* formations. The *Máaz* rock spectra have absorptions centered at 866 and 940 nm, and the rock fragment spectra have NIR absorptions between 900 and 940 nm (Figure 9a). Spectra of in-place *Séítah* formation rocks and mixed regolith rock fragments are characterized by negative NIR slopes (Figure 9b). The *Séítah* spectra also exhibit peak reflectance short of 700 nm, except for one rock fragment (cyan spectrum; Figure 9b), a characteristic shared by the coarse-grained regolith spectra (Figure 8).

4.3. SuperCam LIBS Data

Elemental abundances of the three regolith types were also characterized using SuperCam LIBS analyses. The chemical compositions of the identified regolith types presented are derived from targets that were analyzed by Mastcam-Z for their multispectral properties as well as by SuperCam RMI and LIBS. Utilizing this subset of regolith targets acquired throughout the Campaign, we compared the elemental abundances of the fine-grained, coarse-grained, and mixed types (Figure 10, Table 3). The results obtained indicate two to three major point clouds are visible, due to some expected spot-to-spot scatter within the raster for each target. Table 3 also reports the standard deviation for all laser shots comprising each spot in the LIBS raster for each target.

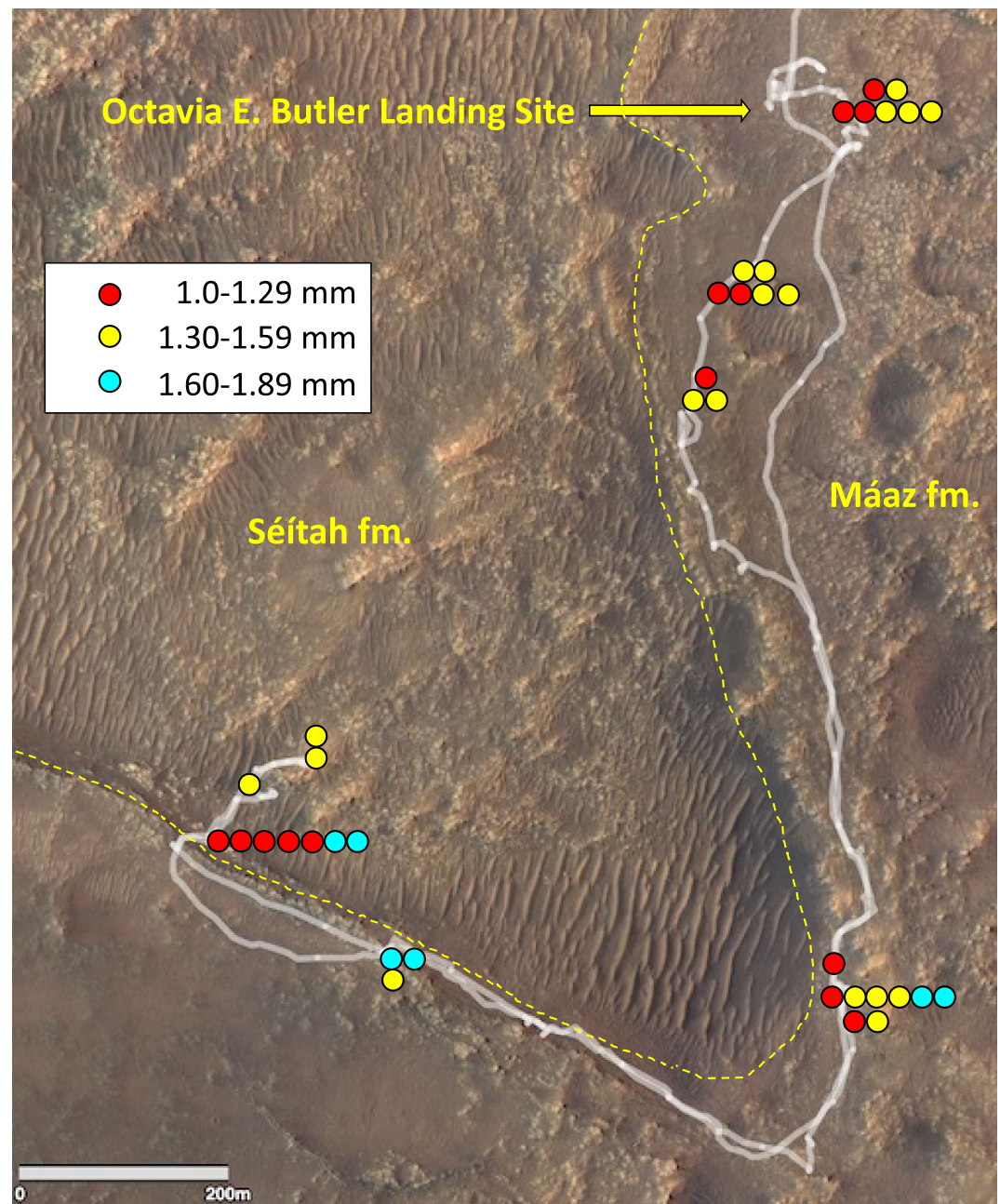


Figure 6. The spatial distribution of average grain sizes of coarse-grained regolith targets across the study area determined by Mastcam-Z, SuperCam Remote Micro Imager, and Wide Angle Topographic Sensor for Operations and eNginering. Regolith targets used for coarse-grained regolith measurements were limited to observations made from specific distance ranges (see Methods). Equivalent instrument—specific maps are contained in Figure S3 in Supporting Information S1. The white line traces the rover traverse, and the yellow dashed line represents the approximate division between the *Máaz* and *Séítah* formations (Sun et al., 2022). Base map is HiRISE IRB (infrared, red, and blue-green filters) color (Ferguson et al., 2020).

The *Sei* target is an example of the fine-grained regolith type, as it predominantly includes grains $<500\ \mu\text{m}$ in diameter (Figure S5b in Supporting Information S1). Its overall chemistry is mafic with minor variations between the raster spots. The largest variations in oxide contents (20%–65%) occur between two raster spots (spots 1 and 4; Table 3); the rest of the chemical variability is $<20\%$. This relative homogeneity is apparent by the tight clustering of *Sei* raster spots within the ternary diagram in Figure 10a; their chemistries fall between the Ca-pyroxene and orthoclase/andesine standards.

Grain roundedness by unit

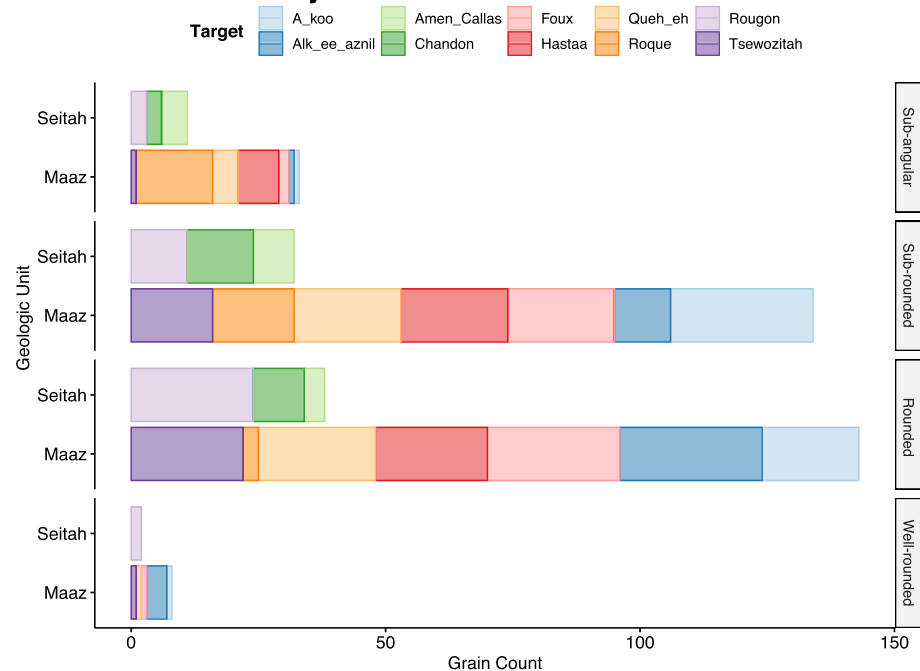


Figure 7. Stacked barplots of grain roundedness determined for coarse-grained regolith grains within the *Séitah* and *Máaz* formations and colored by the target. Though a greater number of regolith targets were analyzed within the *Máaz* formation than the *Séitah* formation, most of the coarse grains examined were subrounded to round for both formations.

Hastaa and *A_koo* represent the coarse-grained regolith type with average compositions enriched in MgO and FeOT relative to the fine-grained regolith (Table 3). *A_koo*, a target where coarse grains are found around the perimeter of a *Máaz* bedrock slab (Figures 1h and 4a, Figure S5a in Supporting Information S1), exhibits a more spot-to-spot variability in chemistry than the fine-grained regolith (Figure 10a). Its overall chemistry is mafic, with most of the spots high in MgO (>16 wt.%) and FeO (>24 wt.%). The remaining spots have elevated SiO₂ and Al₂O₃ contents, indicating that these spots are relatively more felsic (Table 3). *Hastaa* (Figure 1e, Figure S5c in Supporting Information S1), a ripple comprised fine-grained regolith armored by the coarse-grained regolith, also has a more spot-to-spot variability than the fine-grained regolith (Figure 10a). Overall chemistry is mafic, with half of the spots exhibiting high MgO (>24 wt.%) and high FeO (>25 wt.%). The remaining spots have slightly more SiO₂, and variably elevated Al₂O₃, CaO, and/or Na₂O contents. The spot-to-spot variability in chemistry for these targets is not surprising given the intimate mixture of fine and coarse grains, the resolution of the laser beam, and the fact the laser spots hit varying proportions of finer and coarser regolith grains (Figure S5 in Supporting Information S1). The majority of *Hastaa* and *A_koo* grains plot closer to the standards of olivine, serpentine, and pyroxene than does the fine-grained regolith chemistry, consistent with coarse-grained regolith targets having enriched FeOT and MgO compared to fine-grained regolith (Table 3, Figure 10a).

The *Naakih* target (Figures 1i and 3b, Figure S5d in Supporting Information S1) represents the mixed regolith type, enriched in SiO₂ (51.76%_{mean}) and Al₂O₃ (9.42%_{mean}) relative to the fine and coarse-grained regolith (Table 3). Most *Naakih* points are chemically similar to *Nataani*, a nearby bedrock target in the *Máaz* Fm that plots closely to the andesine and orthoclase standards and contains variable Al₂O₃ and SiO₂ relative abundances (Figure 10b). Some of the *Naakih* observations fall closer to the pyroxene standards and overlap the composition of fine-grained regolith target *Sei*. The LIBS raster footprint from *Naakih* (Figure S5d in Supporting Information S1) indicates that the raster spots hit varying proportions of rock fragments and fine-grained regolith.

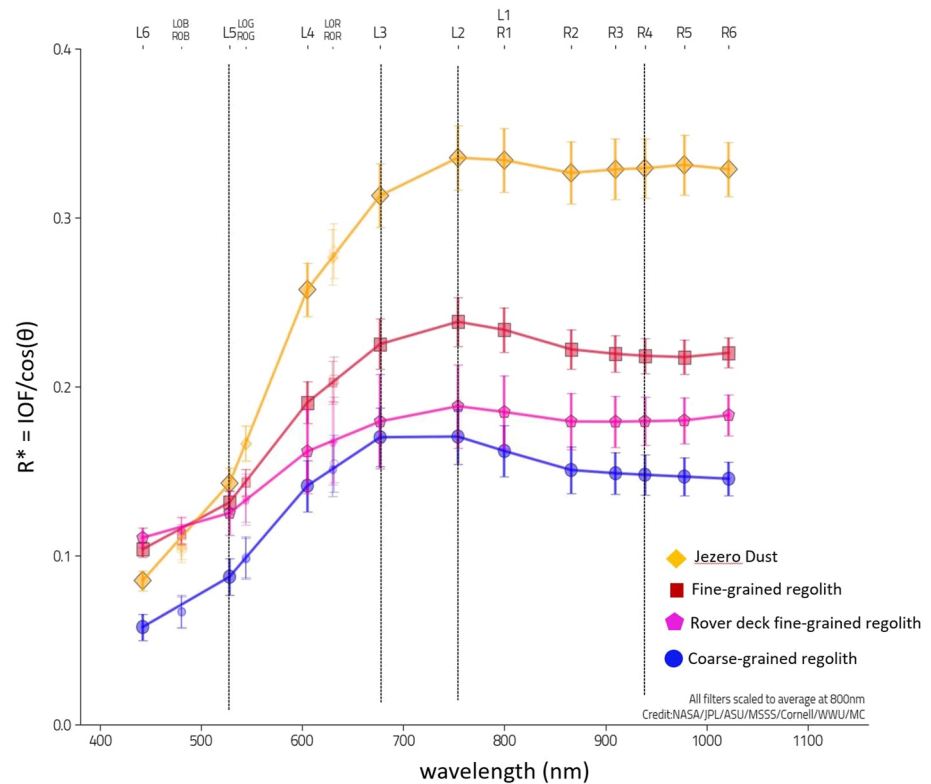


Figure 8. Mastcam-Z spectral averages for fine- and coarse-grained regolith, fine-grained regolith collected on the rover deck from Sol 344, and dust. Vertical lines draw attention to the spectral shape features discussed in the text: 528, 677, 754, and 940 nm.

5. Discussion

5.1. Distinguishing Regolith Types by Chemistry and Mineralogy

Mastcam-Z spectral characteristics vary sufficiently among the different regolith types to differentiate them from each other and from global airfall dust. Some number of nanophase ferric oxides associated with Martian dust are widely found in Martian regolith (Berger et al., 2016; Yen et al., 2005), and images of the regolith from this study (e.g., Figure 2) show the intimate association of dust and regolith. However, each of the regolith types in this study exhibits spectra that are distinct from the average dust spectrum at Jezero (Figure 8). The average dust is brighter (overall higher reflectance values), with stronger ferric iron absorption at 528 nm, weak and narrow absorption at 866 nm, and a steeper red slope as compared to both fine and coarse regolith spectra.

The spectra of fine-grained regolith are distinguished by absorption at 528 nm, a positive (red) slope between 677 and 754 nm, and concave shape in the NIR caused by absorption around 900 nm (Figure 8). These spectral features are consistent with both some ferric oxides and some pyroxenes (Figure 11a). To assess contributions from ferric oxide phases, we compared the strength of spectral features associated with ferric iron in the fine-grained regolith with appropriate laboratory spectra (Figure 12). These ferric-iron spectral features include absorptions at 528 and 866 nm caused by electronic crystal field effects, and the overall “redness” of the spectrum (R^*_{754}/R^*_{442}). These spectral parameters are defined for the Mastcam-Z filter set in Rice et al. (2023).

The broad NIR absorption seen in the fine-grained regolith approximates the ferric iron absorption in goethite, but goethite alone is not a good match in the visible region of the spectrum (Figure 11a). Red, crystalline hematite is not a good match due to the lack of a strong absorption band at 866 nm. The magnitude of ferric iron band depths and overall redness of both red hematite and goethite are greater than that observed in fine-grained regolith (Figure 12). Both JSC Mars-1 and nanophase hematite are similar in spectral shape to the fine-grained regolith of Jezero, with some notable differences. JSC Mars-1, a simulant for Mars regolith composed of weathered volcanic ash from a Hawaiian cinder cone, provides a relevant comparison to fine-grained regolith at Jezero

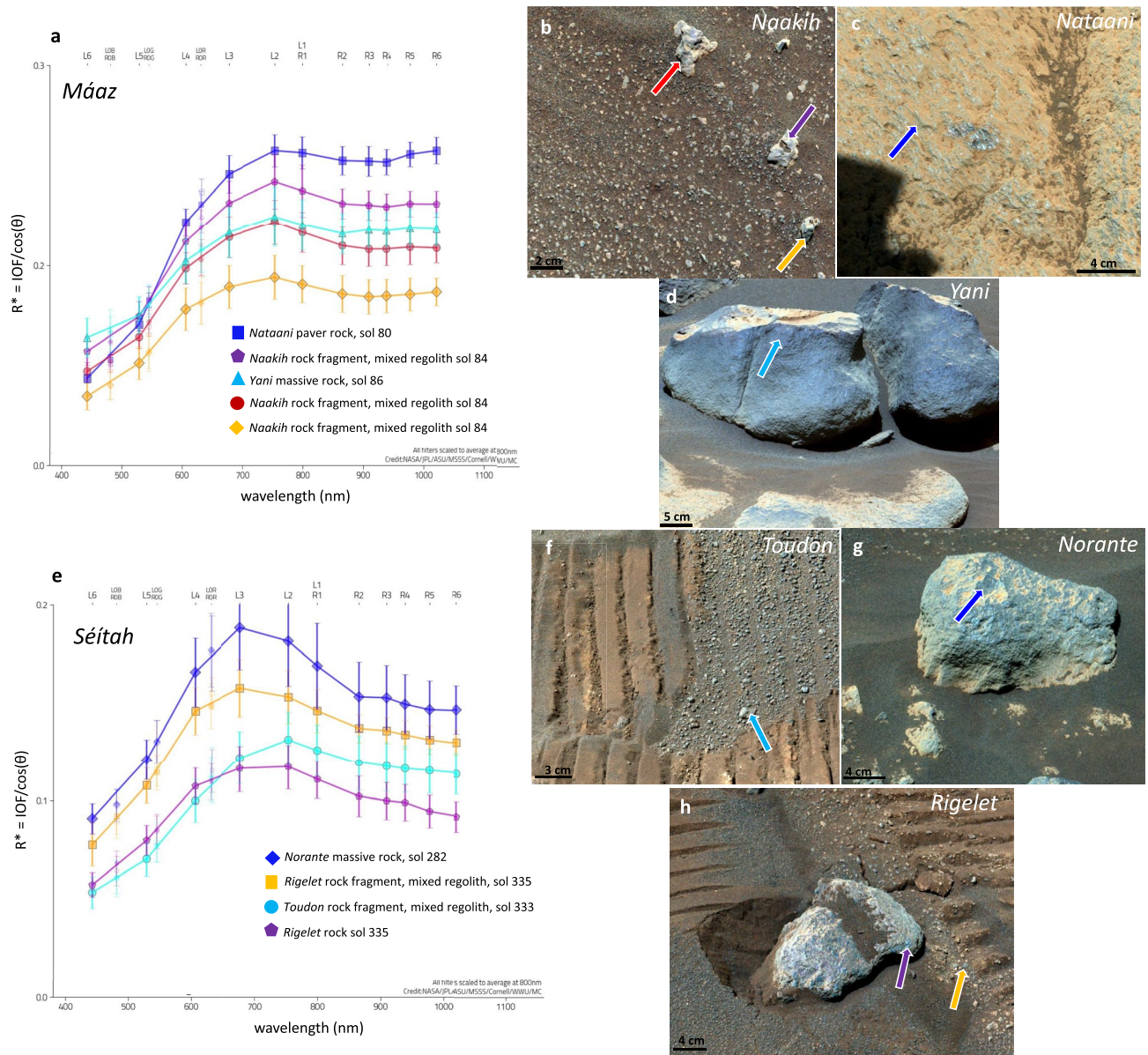


Figure 9. (a) *Máz* formation: mixed regolith rock fragment spectra from (b) *Naakih* (Sol 84, zcam03133) compared to nearby in-place *Máz* formation rocks (c) *Nataani* (Sol 80, zcam03129) and (d) *Yani* (Sol 86, zcam03135). (e) *Séítah* Formation: mixed regolith rock fragment and pebble spectra from (f) *Toudon* (Sol 333, zcam03304) and (h) *Rigelet* (Sol 335, zcam03305) compared to larger *Séítah* rocks (g) *Norante* (Sol 282, zcam03066) and *Rigelet* (Sol 335) nearby. See *Séítah* formation rock spectra in Figure 11. All images are L0 (Bayer) enhanced color. Arrow colors within images correspond to spectrum colors.

as it contains grains <1 mm in size that are compositionally similar to regolith measured by both Viking landers and Pathfinder, with the exception of being Al-enriched, and most of the iron is present as nanophase ferric oxide (Allen et al., 1997). Comparing the ferric iron features between them shows that both JSC Mars-1 and nanophase hematite are slightly redder than the fine-grained regolith, and have peaks extended to longer wavelengths. Nanophase hematite has stronger 528 nm absorption, and JSC Mars-1 has a flatter NIR profile, lacking any hint of a ~900 nm absorption feature. While neither is a perfect match, the presence of the 528 nm absorption feature in the Jezero fine-grained regolith indicates the presence of ferric-iron, and we hypothesize that some of that is coming from the dust component, known to contain nanophase ferric oxides. As described in Section 4.2.1, the recently mobilized fine-grained regolith deposited on the rover deck after the Sol 317 wind event is assumed to be less dusty than fine-grained regolith on the undisturbed surface (represented by the average fine-grained regolith spectrum), which has had more time to accumulate dust. Indeed, Figure 12 shows that the fine-grained material on the rover

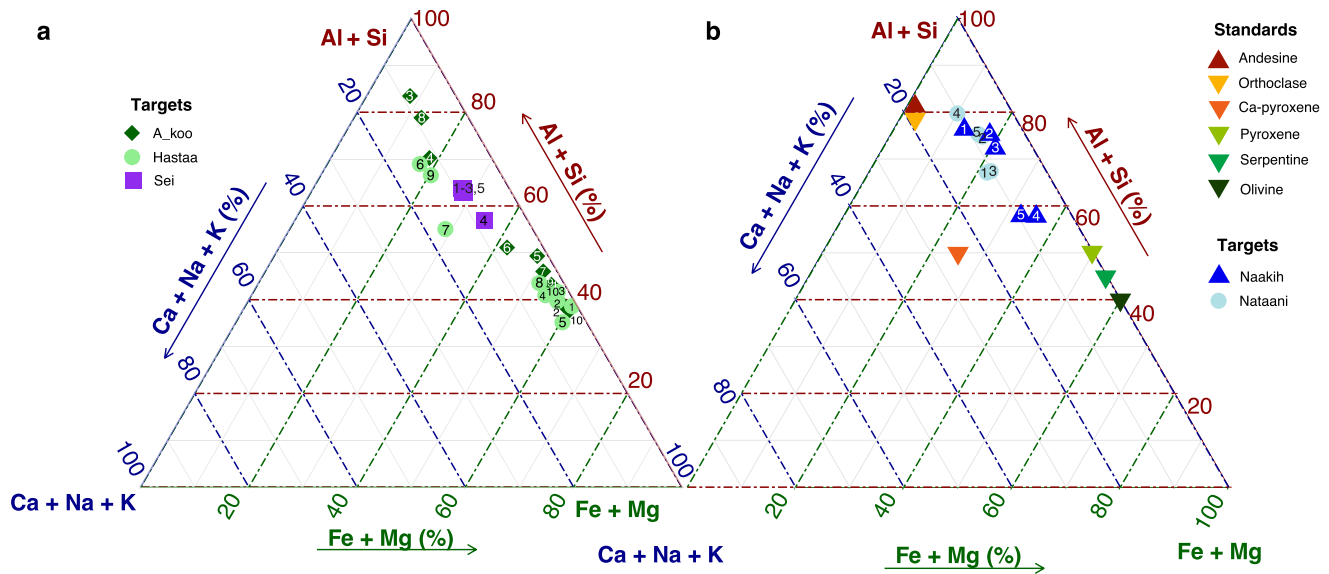


Figure 10. Ternary diagrams of (a) fine- and coarse-grained regolith targets (*Sei*—fine, *Hastaa* and *A_Koo*—coarse) and (b) mixed regolith target *Naakih* (blue) with nearby in-place *Máz* bedrock *Nataani* (light blue). The numbered symbols correspond to the point number in Table 3 and the labeled Remote Micro Imager images in Figure S3 in Supporting Information S1.

deck has weaker ferric iron spectral features than the average fine-grained regolith, which likely corresponds to a decrease in the dust content. Finally, given that the grain sizes of the fine-grained regolith are much smaller than the ROIs sampled, the spectra of fine-grained regolith represent a mixture of mineral phases (similar to JSC Mars-1), some of which are likely to be the primary ferrous iron phases expected based on orbital mapping efforts of Jezero (e.g., Brown et al., 2020; Goudge et al., 2015; B. H. N. Horgan et al., 2020) and detected by SuperCam LIBS and VISIR measurements (Cousin et al., 2022; Mandon et al., 2022a, 2022b). We therefore investigated possible primary phases containing ferrous iron that could contribute to the spectral shape of fine-grained regolith.

The NIR absorption can also be consistent with ferrous iron absorptions in pyroxene, particularly low calcium pyroxenes (LCP), or Fe-rich clinopyroxene, which has absorptions centered between 900 and 950 nm (Cloutis & Gaffey, 1991; Klima et al., 2007), but without the corresponding $\sim 2,000$ nm band, it is difficult to determine a specific pyroxene. This interpretation is consistent with previous multispectral analyses of regolith; for example, Yen et al. (2005) used the 900 nm band in combination with a weak ferric edge (or 528 nm absorption) to interpret a pyroxene component and mafic nature of the fine-grained Gusev soil.

Other data set. also support a pyroxene contribution to the regolith. The diagnostic 2,000 nm pyroxene band is detected in Jezero by the CRISM imaging spectrometer from orbit, and Horgan et al. (2020), using CRISM data to map both low and high Ca pyroxene, showed the region comprising the *Máz* formation as being dominated by clinopyroxene. Mandon et al. (2022a, 2022b) suggested that an intermediate Ca-pyroxene was a good candidate to explain some of the SuperCam infrared spectra of fine-grained regolith in the *Máz* formation. Using both SuperCam LIBS and VISIR data, Cousin et al. (2022) and Mandon et al. (2022b) have shown that the fine-grained regolith at Jezero is a mixture of minerals containing pyroxene and plagioclase and has a more felsic composition than the coarse-grained regolith. Taken together, the data indicate that the spectra of fine-grained regolith of the Jezero crater floor are a mixture of material containing dust and other primary igneous phases. A ferric iron component indicated by the 528 nm absorption could be contributed by nanophase hematite present in the dust or as a weathering product of local rocks, and pyroxene is a likely primary component given the position of the NIR absorption, and the weak magnitude of ferric iron spectral features observed in fine-grained regolith overall.

The spectra of coarse-grained regolith are distinguished by flat to negative slopes both between 677 and 754 nm and through the NIR; these features differentiate coarse-grained regolith spectra from fine-grained regolith spectra (Figures 8 and 11b). This spectral shape is consistent with ferrous iron absorptions around 1,000 nm associated with volcanic glass and olivine (Figure 11b). Coarse-grained regolith also plots near olivine and basaltic glass in the parameter space detailed below (Figure 13). Olivine has been detected both from orbit and in situ as a dominant component of the *Bastide* and *Issole* members of the *Sítah* formation (Farley et al., 2022; Liu

Table 3
Elemental Chemistry (Major Oxide Composition) of SuperCam Laser-Induced Breakdown Spectroscopy Targets^a

Target ^b	Point	SiO ₂ ^c	TiO ₂	Al ₂ O ₃	FeO _T	MgO	CaO	Na ₂ O	K ₂ O	Total
Fine-grained type										
<i>Sei</i>	1	41.53 ± 3.93	0.68 ± 0.1	8.57 ± 1.06	13.8 ± 2.41	5.67 ± 1.48	4.24 ± 0.59	1.39 ± 0.43	0.74 ± 0.54	76.62
	2	40.72 ± 3.29	0.68 ± 0.07	8.21 ± 1.23	14.04 ± 1.62	5.73 ± 1.37	4.12 ± 0.62	1.53 ± 0.46	0.9 ± 0.55	75.93
	3	42.4 ± 3.44	0.66 ± 0.08	7.91 ± 0.98	14.39 ± 3	6.14 ± 1.69	3.98 ± 0.7	1.6 ± 0.48	0.9 ± 0.59	77.98
	4	40.87 ± 3.16	0.51 ± 0.15	7.12 ± 1.76	13.67 ± 5.26	10.82 ± 6.3	3.9 ± 0.52	1.42 ± 0.29	1.22 ± 0.61	79.53
	5	41.45 ± 3.8	0.64 ± 0.08	8.13 ± 1.11	13.44 ± 4.18	5.91 ± 1.78	3.98 ± 0.71	1.31 ± 0.41	0.9 ± 0.69	75.76
	Average	41.39	0.63	7.99	13.87	6.85	4.06	1.45	0.93	
Coarse-grained type										
<i>A koo</i>	1	47.65 ± 2.72	0.01 ± 0.05	1.49 ± 1.2	24.08 ± 3.64	27.34 ± 1.37	1.6 ± 0.44	1.13 ± 0.29	0 ± 0.29	103.3
	2	44.08 ± 2.29	0.05 ± 0.2	3.22 ± 2.08	36.46 ± 7.43	26.3 ± 8.2	1.7 ± 1.07	0.99 ± 0.39	0.03 ± 0.43	112.83
	3	62.23 ± 2.19	0.38 ± 0.14	12.5 ± 1.2	6.49 ± 1.72	0.84 ± 0.3	1.45 ± 0.48	3.66 ± 0.24	3.1 ± 0.63	90.65
	4	49.58 ± 1.46	0.49 ± 0.07	13.05 ± 1.49	14.82 ± 1.46	1.62 ± 0.37	5.13 ± 0.7	3.72 ± 0.3	0.4 ± 0.41	88.81
	5	45.47 ± 6.47	0.01 ± 0	2.49 ± 1.48	26.1 ± 2.82	16.32 ± 1.1	1.5 ± 0.49	0.35 ± 0.1	0 ± 0.03	92.24
	6	44.75 ± 2.65	0.69 ± 0.09	7.78 ± 1.08	30.85 ± 6.17	9.87 ± 1.68	3.78 ± 0.61	2.26 ± 0.47	0.35 ± 0.52	100.33
	7	45.86 ± 3.58	0.05 ± 0.15	3.45 ± 1.55	35.64 ± 5.17	15.76 ± 4.62	1.7 ± 0.72	0.89 ± 0.3	0 ± 0.22	103.35
	8	55.17 ± 5.3	0.5 ± 0.1	14.45 ± 3.31	8.23 ± 6.06	2.12 ± 2.02	3.7 ± 1.07	2.16 ± 0.64	1.48 ± 0.61	87.81
	9	44.56 ± 2.62	0.36 ± 0.23	4.98 ± 2.45	26.51 ± 6.16	25.47 ± 8.27	2.58 ± 1.13	1.26 ± 0.42	0 ± 0.57	105.72
	10	45.64 ± 2.31	0.05 ± 0.17	0.95 ± 2.19	36.9 ± 6.77	28.77 ± 6.14	1.57 ± 0.99	0.64 ± 0.3	0 ± 0.26	114.52
	Average	48.50	0.26	6.44	24.61	15.44	2.47	1.71	0.54	
<i>Hastaa</i>	1	42.77 ± 2.42	0.01 ± 0	2.33 ± 0.92	26.14 ± 2.67	31.6 ± 1.02	0.76 ± 0.46	0.3 ± 0.11	0.01 ± 0.03	103.92
	2	44.11 ± 2.76	0.24 ± 0.27	2.15 ± 2.8	27.79 ± 3.72	28.18 ± 9.81	2.16 ± 1.5	0.97 ± 0.51	0.58 ± 0.46	106.18
	3	44.19 ± 4.66	0.02 ± 0.03	3.39 ± 1.46	27.64 ± 2.72	26.27 ± 2.11	1.67 ± 0.67	0.55 ± 0.2	0 ± 0.24	103.73
	4	43.7 ± 2.59	0.41 ± 0.29	5.06 ± 2.56	29.49 ± 4.97	24.87 ± 10.68	3.55 ± 1.37	1.26 ± 0.6	0.53 ± 0.41	108.87
	5	34.7 ± 8.35	0.01 ± 0	1.78 ± 1.31	30.02 ± 6.05	24.2 ± 5.5	2.13 ± 0.61	2 ± 0.23	0.47 ± 0.56	95.31
	6	46.29 ± 2.11	0.51 ± 0.27	18.3 ± 2.93	9.57 ± 1	4.11 ± 0.72	6.09 ± 0.73	4.04 ± 0.59	1.66 ± 3.3	90.57
	7	47.85 ± 1.66	0.52 ± 0.07	5.42 ± 2.3	10.23 ± 3.37	12.12 ± 1.72	13.34 ± 3.29	0.57 ± 0.4	0 ± 0.17	90.05
	8	49.5 ± 3.01	0.04 ± 0.17	1.98 ± 1.91	27.94 ± 2.3	24.75 ± 7.49	3.99 ± 1.14	1.04 ± 0.4	0 ± 0.21	109.24
	9	49.79 ± 2.12	0.35 ± 0.15	19.09 ± 1.77	9.97 ± 1.19	6.9 ± 1.88	5.9 ± 0.39	5.46 ± 0.43	0.56 ± 0.4	98.02
	10	43.12 ± 2.34	0.05 ± 0.28	3.81 ± 2.15	25.47 ± 5.39	26.85 ± 9.61	2.57 ± 1.43	0.85 ± 0.54	0.19 ± 0.42	102.91
	Average	44.60	0.22	6.33	22.43	20.99	4.22	1.70	0.40	
Mixed type										
<i>Naakih</i>	1	52.24 ± 2.22	0.72 ± 0.09	13.65 ± 2.9	9.28 ± 4.89	1.66 ± 0.32	3.66 ± 0.68	3.9 ± 0.24	1.1 ± 0.5	86.21
	2	59.4 ± 7.33	0.5 ± 0.14	9.32 ± 1.1	15.86 ± 5.31	1.62 ± 0.41	1.6 ± 1.27	2.87 ± 0.55	1.74 ± 0.77	92.91
	3	54.8 ± 6.27	0.52 ± 0.07	9.11 ± 1.45	16.12 ± 2.63	2.5 ± 2.15	1.8 ± 0.94	2.76 ± 0.66	1.84 ± 0.71	89.45
	4	44.97 ± 2.44	0.51 ± 0.11	5.63 ± 1.62	13.1 ± 6.63	12.57 ± 6.16	3.78 ± 0.96	1.24 ± 0.17	0.46 ± 0.55	82.26
	5	47.39 ± 4.17	0.67 ± 0.1	9.39 ± 2.23	29.36 ± 7.12	3.5 ± 2.21	4.55 ± 0.5	3.39 ± 0.61	0.65 ± 0.44	98.9
	Average	51.76	0.58	9.42	16.74	4.37	3.08	2.83	1.16	
Rock										
<i>Nataani</i>	1	53.4 ± 2.49	0.48 ± 0.11	7.93 ± 1.26	9.51 ± 3.22	1.25 ± 0.28	1.59 ± 0.49	1.69 ± 0.39	3.36 ± 0.53	79.2
	2	48.7 ± 1.78	0.04 ± 0.01	18.9 ± 1.92	17.6 ± 3.24	2.37 ± 0.37	6.51 ± 0.51	4.35 ± 0.39	0.25 ± 0.45	98.7
	3	51.0 ± 1.79	0.04 ± 0.08	22.7 ± 1.63	11.0 ± 5.41	1.77 ± 0.34	5.71 ± 0.32	4.59 ± 0.34	0.71 ± 0.35	97.5
	4	47.9 ± 2.02	0.4 ± 0.17	15.9 ± 1.23	10.7 ± 2.51	1.55 ± 0.33	5.54 ± 0.13	3.51 ± 0.34	1.09 ± 0.63	86.6
	5	41.5 ± 2.08	0.39 ± 0.06	4.12 ± 0.92	49.8 ± 7.6	1.42 ± 0.65	3.41 ± 0.71	1.17 ± 0.44	0.08 ± 0.26	102

Table 3
Continued

Target ^b	Point	SiO ₂ ^c	TiO ₂	Al ₂ O ₃	FeO _T	MgO	CaO	Na ₂ O	K ₂ O	Total
	6	61.0 ± 3.48	0.62 ± 0.05	11.6 ± 1.08	6.3 ± 1.59	1.01 ± 0.18	2.35 ± 0.71	4.3 ± 0.38	3.31 ± 0.42	90.4
	7	58.2 ± 3.64	0.77 ± 0.06	7.52 ± 1.07	25.0 ± 7.81	1.66 ± 0.25	1.74 ± 0.39	3.05 ± 0.4	2.56 ± 0.3	101
	8	43.6 ± 1.81	0.64 ± 0.03	7.92 ± 1.12	12.8 ± 1.32	4.9 ± 0.79	4.59 ± 0.48	2.51 ± 0.39	0.99 ± 0.43	78
	9	56.7 ± 3.61	0.64 ± 0.08	10.2 ± 2.54	8.94 ± 1.75	1.65 ± 0.55	3.37 ± 1.25	2.97 ± 0.54	2.23 ± 0.51	86.8
	10	44.6 ± 1.92	0.67 ± 0.01	10.6 ± 1.2	12.5 ± 1.37	5.68 ± 0.92	5.06 ± 0.73	3.6 ± 0.29	0.7 ± 0.34	83.3
	Average	50.66	0.47	11.74	16.42	2.33	3.99	3.17	1.53	

^aAll targets are within the *Mááz* formation. ^bSols of targets: *Sei* (Sol 84), *A koo* (Sol 72), *Hastaa* (Sol 106), *Naakih* (Sol 84), and *Nataani* (Sol 75). ^cAll oxides reported in wt.% with standard deviation values (±) for all laser shots comprising the point.

et al., 2022; Wiens et al., 2022). Mastcam-Z spectra of olivine-rich rocks in *Séítah* share spectral characteristics with the coarse-grained regolith spectra (Figure 11b; Bell et al., 2022; Rice et al., 2022a, 2023), making olivine a better interpretation for a major component of the coarse grains. SuperCam VISIR spectra from the Crater Floor Campaign, which are described in detail in other studies (Beyssac et al., 2021; Cousin et al., 2022; Mandon et al., 2022a, 2022b; Wiens et al., 2021) further support olivine as the source of the flat to negative NIR slope in Mastcam-Z spectra. SuperCam visible spectra (0.4–0.85 μm) of *Séítah* bedrock and coarse-grained regolith exhibit a negative slope at >0.7 μm, and near infrared spectra (1.3–2.6 μm) exhibit a steep reflectance drop off at <1.8 μm (Mandon et al., 2022a, 2022b; Wiens et al., 2021). Both characteristics are consistent with the broad, ferrous 1,000 nm absorption commonly attributed to olivine.

We evaluated the entire Mastcam-Z crater floor regolith spectral database using spectral parameters identified as diagnostic of the regolith components to better understand spectral trends and identify endmembers. Rice et al. (2023) details the function and calculation of the spectral parameters employed here. Figures 13 and 14 plot all the nearfield regolith spectra in a parameter space that distinguishes olivine-like spectra from the pyroxene/ferric-iron like spectra. The peak reflectance is sensitive to the 754 nm/677 nm ratio on the x-axis and the 1,022 nm/866 nm ratio quantifies the magnitude of the NIR absorption on the y-axis. This places olivine-like spectra to the lower left, and pyroxene or ferric oxide-like spectra to the upper right in the plot. All points in Figure 13 are color-coded by the strength of the 528 nm band depth, and by grain size class in Figure 14.

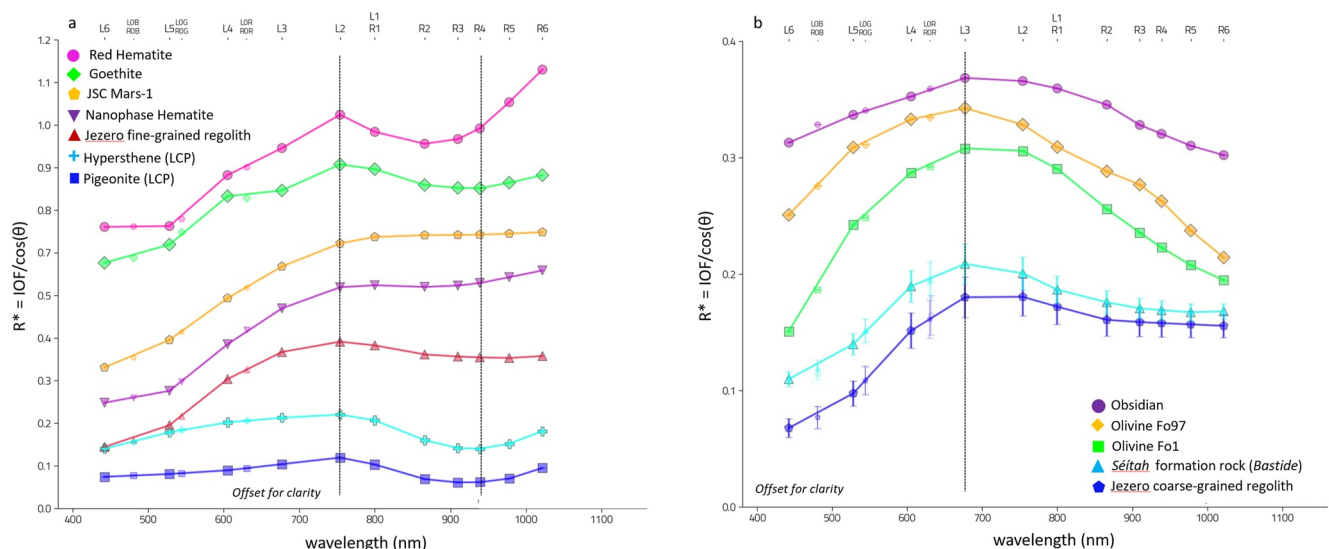


Figure 11. (a) Jezero average fine-grained regolith (scaled ×2) shown with laboratory spectra resampled to Mastcam-Z wavelengths and offset for clarity. The vertical lines at 754 and 940 nm represent the maximum reflectance and the minimum of the near-infrared (NIR) feature in the Jezero fine-grained regolith. (b) Jezero average coarse-grained regolith shown with laboratory spectra re-sampled to Mastcam-Z wavelengths. The vertical line at 677 nm is noting the peak reflectance of these materials, followed by flat to negative NIR slopes. Also shown is a representative spectrum from the olivine-rich *Séítah* bedrock for comparison with Sol 213 zcam03235 (Bell et al., 2022).

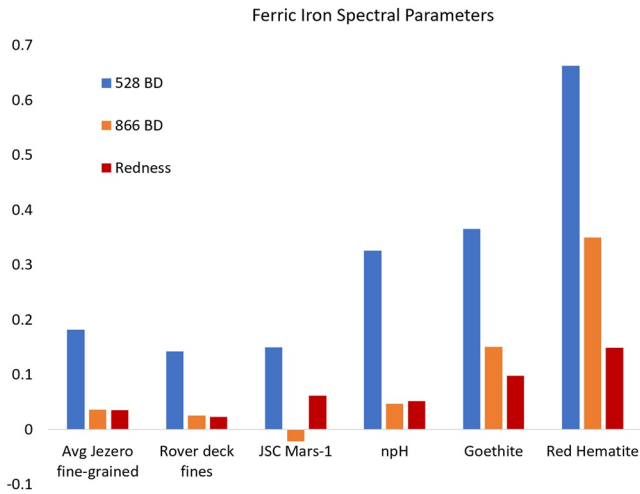


Figure 12. Comparison of ferric iron spectral parameters including 528 nm band depth (BD), 866 nm BD, and overall redness of the spectrum (R_{754}^*/R_{442}^*) for the average fine-grained regolith and less dusty fine-grained regolith on the rover deck with laboratory spectra for JSC Mars-1, nanophase hematite (npH) and red, crystalline hematite. Redness values were uniformly scaled down (divided by 100) to plot alongside band depths.

Endmember spectra from this graph are also shown in Figure 15 representing the more pyroxene or ferric oxide like fine-grained regolith and the coarser, olivine-like grains.

Figure 13 shows that the strength of the 528 nm band, used to assess a ferric iron contribution, varies between regolith types. Stronger 528 nm band depths track toward the upper-right, away from the coarser-grained, olivine-like spectra, showing that the finer-grained material has a stronger ferric-oxide component, consistent with the observation that it is often intimately mixed with dust. The fine-grained regolith collected on the rover deck is labeled as well and is consistent with other fine-grained regolith targets on the natural surface. The most olivine-like spectra from regolith targets plot near the laboratory spectra for basaltic glass and Fo97 olivine. They represent both the coarse grains armoring bedforms and coarse gray grains that collected around the base of rocks. Specific targets *Niyol*, *Sey dey yilkid*, *Foux*, and *Raton* labeled on the plot are shown in Figures 1b, 1g, 1d and 1k and two of these spectra are shown as endmembers in Figure 15. The most olivine-like spectra in the entire Mastcam-Z spectral database from the Crater Floor Campaign are from the abraded surfaces of *Séítah* formation rocks, and plot closer to Fo66 olivine (Bell et al., 2022; Rice et al., 2022a). Using CRISM data, Brown et al. (2020) constrained the Fo number for the *Séítah* region to between Fo44 and Fo66, and LIBS data of *Séítah* rocks agree (Wiens et al., 2022). The coarse-grained regolith shown here to be consistent with an olivine composition could be sourced locally from the *Séítah* rocks, though

the crater floor regolith has been re-worked by aeolian processes. Further, with olivine observed from orbit in many locations in and near Jezero crater (e.g., Hoefen et al., 2003; Mustard et al., 2005; Tornabene et al., 2008), contributions from outside Jezero crater cannot be ruled out.

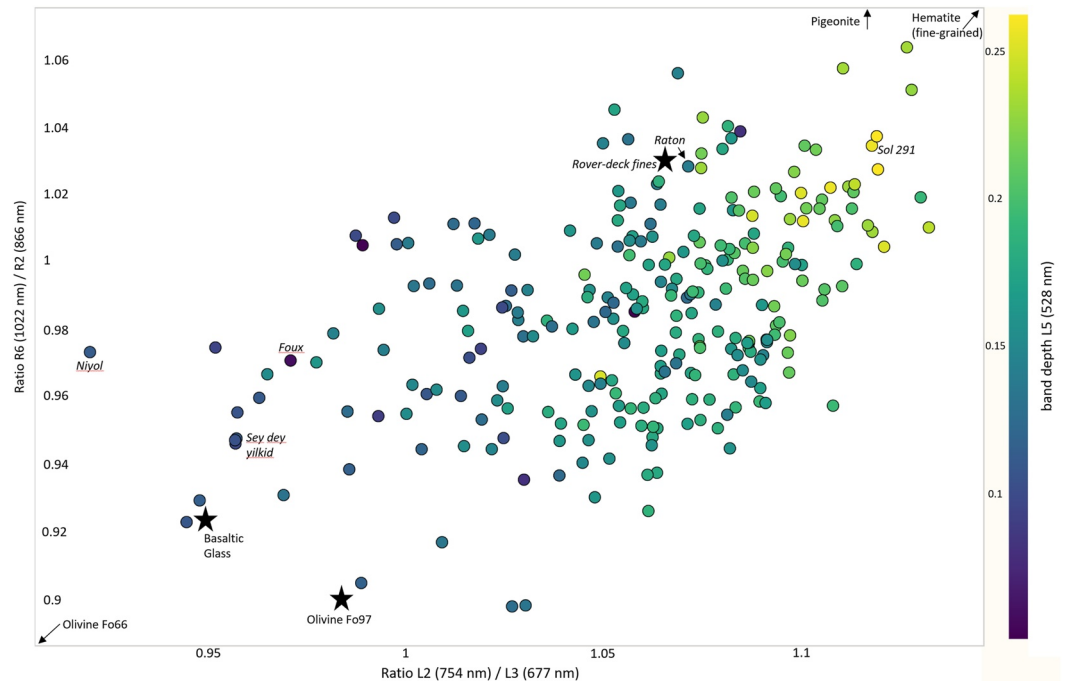


Figure 13. Regolith targets plotted in spectral parameter space diagnostic of more olivine-like spectra (toward the lower left) and more pyroxene/ferric iron-like spectra (toward the upper right). Each target is color-coded by the strength of the 528 nm absorption, showing that stronger 528 nm band depths track toward the upper right. Laboratory spectra, and the rover deck fine-grained spectra from Sol 344 are labeled with black stars. The other labeled targets are shown in Figures 1b, 1d, 1g and 1k, and some of these representative endmember spectra are shown in Figure 15.

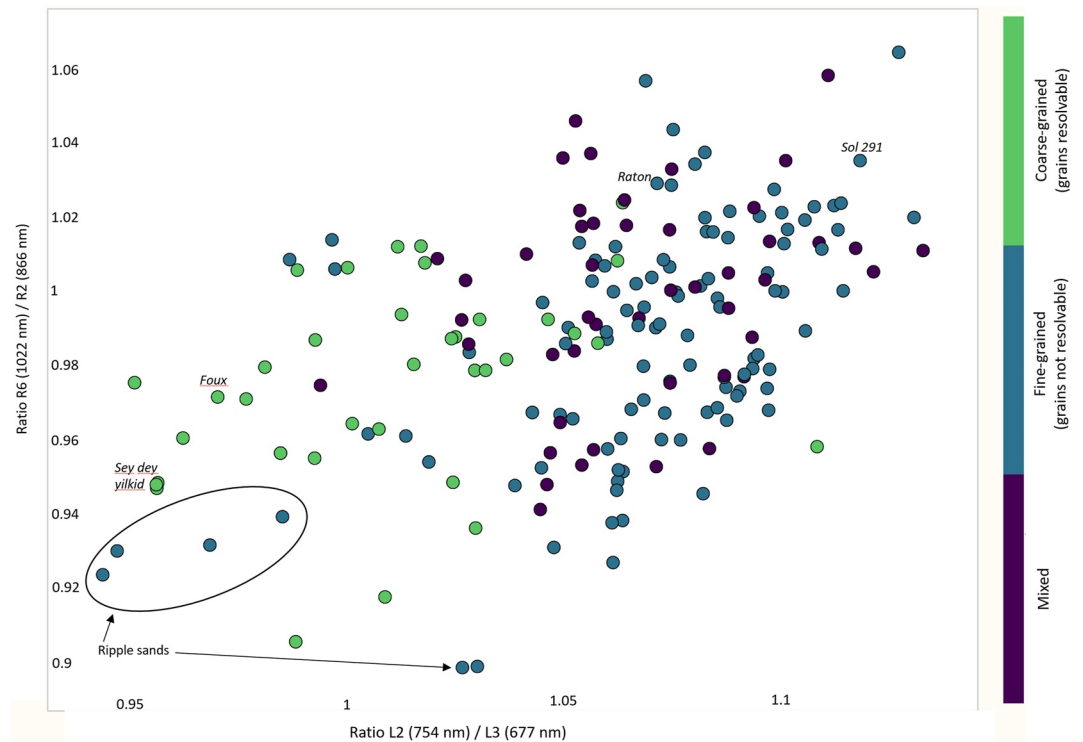


Figure 14. Regolith targets plotted in spectral parameter space diagnostic of more olivine-like spectra (toward the lower left) and more pyroxene/ferric iron-like spectra (toward the upper right). Data points are color-coded according to their associated grain size. Labeled targets are shown in Figures 1b, 1d, 1g and 1k, and these representative endmember spectra are shown in Figure 15.

Figure 14 illustrates how the grain-size association (fine, coarse, and mixed) falls into the same spectral parameter space that delineates compositional endmembers. Finer grained and mixed regolith trends toward the pyroxene/ferric oxide end of the graph, and coarser grained regolith, including bedform sand, trends toward the olivine side of the graph, consistent with the spectral averages shown for these components. The four targets circled in the lower left were classified as fine-grained, but they are bedform sands. Following our guidelines for measuring grain size, the combination of focal length and distance of these targets did not allow for individual grains to be resolved.

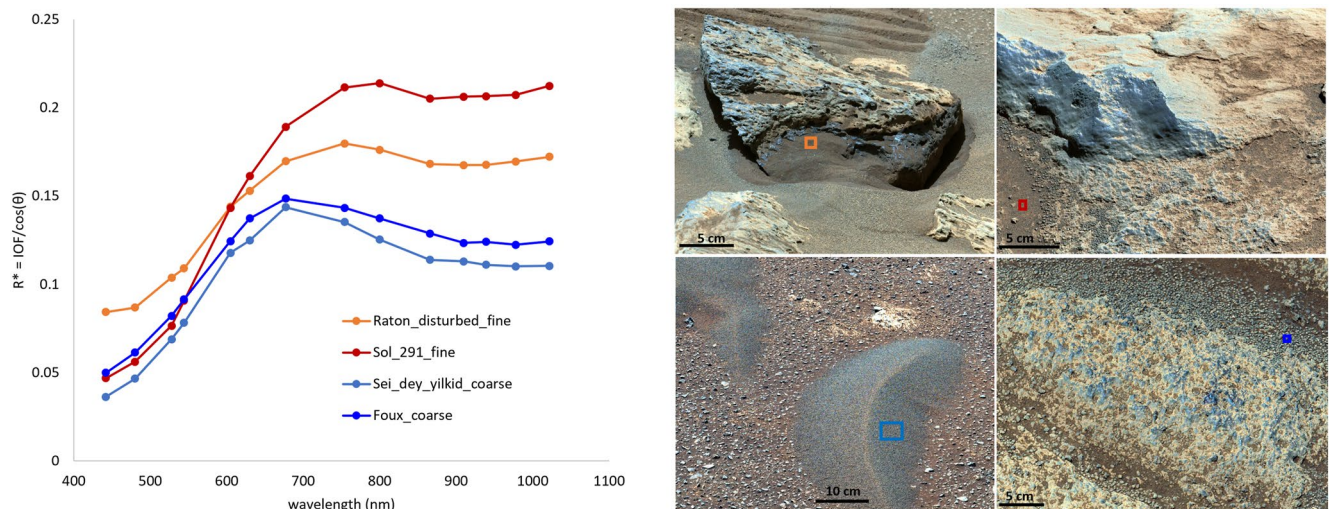


Figure 15. Representative endmember spectra for points labeled in Figures 13 and 14.

As discussed in Section 4.2.1, Figure 9 illustrates the overall similarity between the rock fragments and pebbles present in the mixed regolith and neighboring in-place unit rocks. Mastcam-Z spectra of *Máaz* formation rocks reported elsewhere (Bell et al., 2022; Farley et al., 2022; B. Horgan et al., 2022; Rice et al., 2022a) are characterized by peak reflectances at 754 nm and NIR absorptions that fall between 866 and 940 nm. The similarity in the presence and position of absorptions between the bedrock and rock fragment spectra in *Máaz* shows the idea that the fragments are eroded from local bedrock (Figure 9a). Similarly, *Sétah* bedrock and most *Sétah* rock fragment spectra share peak reflectance short of 700 nm and a negative NIR slope, consistent with the presence of olivine, as discussed for the coarse-grained regolith. The single rock fragment spectrum with a reflectance peak shifted to longer wavelengths (cyan spectrum; Figure 9e) is consistent with a weathered olivine. Olivine-rich rocks with weathering rinds have peak reflectances shifted to longer wavelengths, followed by the characteristic 1,000 nm band, and this spectral behavior has been observed in the olivine-rich *Sétah* bedrock as well (Curtis et al., 2022; Rice et al., 2023). This spectral shape was also observed in the “olivine basalt sand” at the Meridiani landing site (Soderblom et al., 2004) and the Bagnold Dune sands at Gale crater (Lapotre et al., 2017).

SuperCam LIBS observations provide further insight into the compositional differences between the regolith types (Figure 10). There is spot-to-spot consistency of the chemistry within the fine-grained regolith target *Sei* (Figure 10a). We interpret this to be a result of the fine-grained regolith predominately being comprised of grains small relative to the size of the SuperCam laser beam. Thus, each raster spot effectively provides a bulk chemistry measurement of the fine-grained regolith. This suggests that fine-grained regolith is an intimate and relatively homogenous mixture of minerals. The fine-grained regolith has a more felsic composition than coarse-grained regolith, pushing it toward the feldspars and Ca-rich pyroxene on the ternary diagram (Figure 10a, Table 3). The LIBS chemistry is consistent with the SuperCam infrared spectrometer results, which demonstrate that an intermediate Ca-pyroxene is consistent with the fine-grained regolith spectra (Mandon et al., 2022b). The low totals (~75%–80%; Table 3) of the fine-grained target *Sei* can be attributed to the presence of other components such as CO₂, SO₃, Cl, H₂O, P₂O₅, and MnO (Wiens et al., 2022). The presence of phases containing these components could indicate chemical alteration products within the fine-grained regolith; however, identifying these phases would require additional work beyond this study to investigate. The average elemental composition for coarse-grained regolith has higher FeO_T and MgO than fine-grained regolith, and the higher totals (~88%–112%) are less indicative of possible alteration components. The elevated FeO_T and MgO values are consistent with ferrous-iron silicate minerals as evidenced by the coarse-grained regolith chemistries plotting near olivine, serpentine, and pyroxene standards on the ternary diagram (Figure 10a). As expected, there is variability in the chemistry of the coarse-grained targets given the intimate association of fine- and coarse-grained regolith types within *Hastaa* and *A Koo* at the scale of the SuperCam LIBS laser beam (Figure 3a, Figures S5a and S5c in Supporting Information S1), as each laser spot did not land solely on a coarse grain. Further, shot-to-shot variability (~30 shots completed for each laser spot) due to possible heterogeneous grain composition or potential on/off-grain effects might also contribute to the spot-to-spot variability (David et al., 2021). Given the chemical variability of these targets, we evaluated chemical trends via the ternary diagram (Figure 10, Table 2), and found that targets incorporating the coarse grains such as *Hastaa* and *A Koo* are enriched in Fe and Mg, locating them near olivine, serpentine, and pyroxene standards in composition. Thus, the LIBS chemistry data provides further support for the presence of olivine within the coarse-grained regolith.

Comparing the LIBS data of *Naakih* and *Nataani* (Figure 10b) shows that the chemistry variation between local in-place *Máaz* bedrock raster spots and rock fragments in the *Máaz* mixed regolith is very similar, and supports the hypothesis that the larger fragments of the mixed-type regolith are eroded from local bedrock. Several of the *Naakih* (mixed regolith) points plot close to *Nataani* (in-place *Máaz* bedrock) and the others plot near *Sei*, the fine-grained regolith target, consistent with a mix of locally derived rock fragments and fine-grained regolith.

5.2. Evaluating Implications of Grain Size and Roundedness

5.2.1. Grain Size Variations Among Techniques

Utilizing three imagers with three different viewing geometries relative to a target means that two-dimensional measurements (long axis as seen by the imager) are subject to three-dimensional variability of grain shape (Figure 16). We found some variation between average grain sizes derived from different imagers of the same target (Table 1, Figure 5). The magnitudes of differences between average grain sizes derived from different imagers on the same target fell between 0.05 and 0.25 mm, most commonly around ±0.1 mm. Average grain sizes

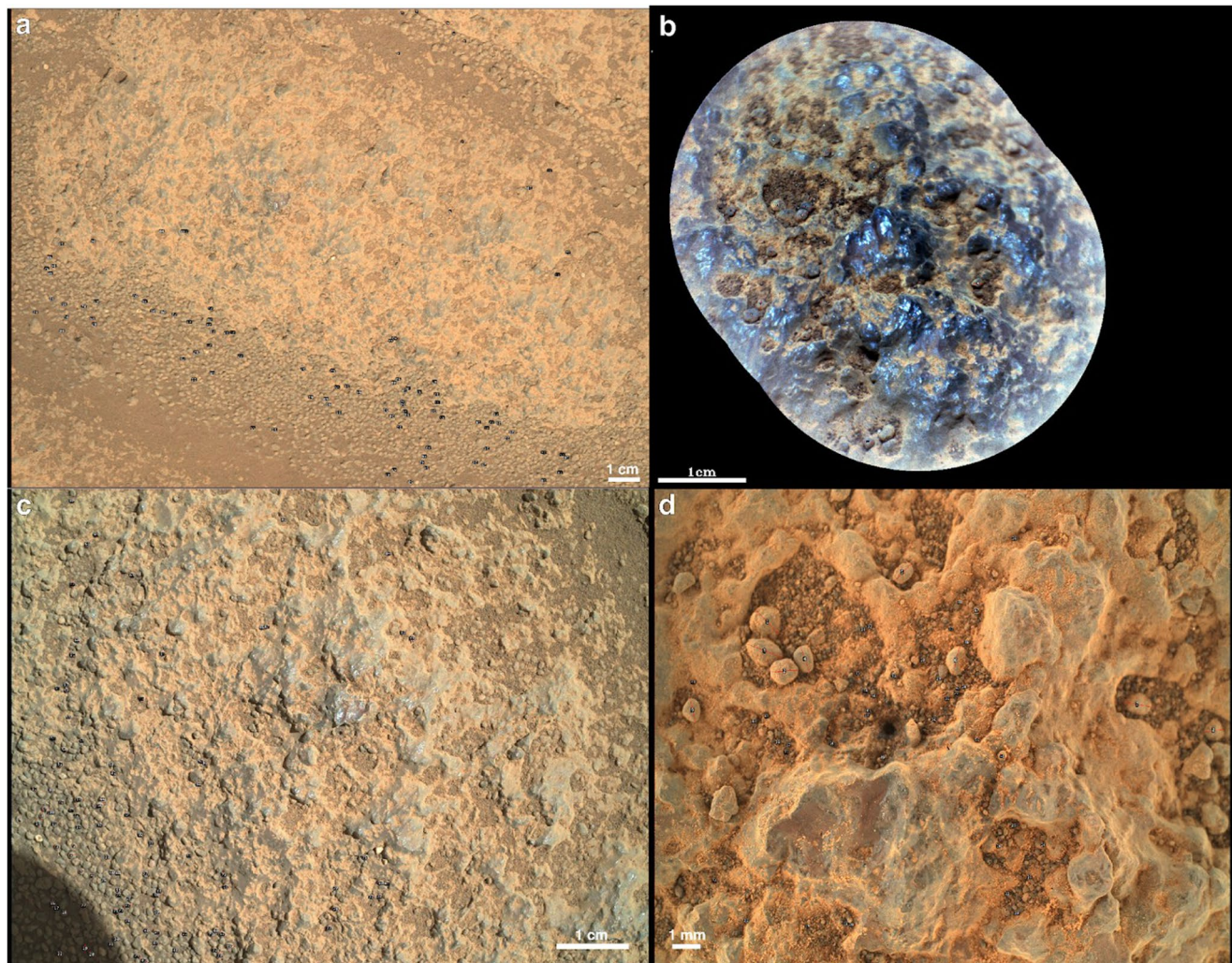


Figure 16. Imaging of the *Foux* target via multiple imaging instruments. (a) Mastcam-Z Z110 (Sol 138, zcam03181)—rotated relative to the same image in Figure 1g to align with the other panels in this figure, (b) SuperCam Remote Micro Imager mosaic, Gaussian color stretch (Sol 138), (c) Wide Angle Topographic Sensor for Operations and eNginneering (WATSON) 25 cm standoff (Sol 139, SIF_0139_0679287794_007EBY_N0051812SRLC02500_0000LMJ01), (d) WATSON 4 cm standoff focus merge (Sol 140, S11_0140_0679334136_035ECZ_N0051812SRLC00003_000095J05). Measured grains denoted by black labels and red lines.

determined by WATSON trend larger than those determined by Mastcam-Z and RMI images; there is no consistent offset direction between Mastcam-Z and RMI-determined averages (Figure 5). The largest difference in average grain size between techniques (0.25 mm) occurred on target *Tsewozith* with grains measured by the same operator in a WATSON image and SuperCam RMI mosaic (Table 1, Figure 5). The same magnitude and direction (WATSON > RMI by 0.3 mm ($n = 32$)) of offset between average grain size derived from WATSON and RMI for *Tsewozith* was found when measurements were limited to grains that could be correlated one-to-one between images (Figure S6 in Supporting Information S1). The consistency of the magnitude and direction of offset between averages derived from different instruments, whether derived from all grains available within images or only identically correlated grains, provides confidence that the former effectively represents inter-instrument variability. While these 0.05–0.25 mm differences in average grain sizes exist between techniques, the range (smallest to largest) of grain sizes among techniques within a single target is consistent (Figure 5). Further, the range and spatial distribution of average grain size across the study area does not change if we limit our grain size measurements to only one image source (Figures S2 and S3 in Supporting Information S1). These consistencies across the data set support that we measured a sufficiently substantial number of grains within each image to appropriately capture the intra- and inter-target variability in grain size. Thus, we believe that the measurement differences between techniques do not affect the conclusions of this work.

5.2.2. Linkages to Séítah

With mineralogical and chemical links apparent between the coarse-grained regolith and *Séítah* formation bedrock, we investigated if there was also a grain size link between them. We measured the long axes of olivine grains in four *Séítah* bedrock targets (Figure 5) using RMI images acquired from a distance range (2.0–4.1 m) comparable to the distance from which the coarse-grained regolith measurements were made. We measured between 53 and 104 grains in each bedrock target. Classification of the bedrock grains as olivine was supported by measurements from multiple techniques in abraded patches within *Séítah* bedrock that included such grains (Bell et al., 2022; Liu et al., 2022; Scheller et al., 2022; Wiens et al., 2022). The long axes of the olivine grains in the four bedrock targets ranged from 0.48 to 2.54 mm ($N = 304$). This range coincides with the range of olivine grain long axes (0.48–2.34 mm, $N = 1,416$) measured across 11 *Séítah* bedrock targets made in order to investigate *Séítah* formation models from the perspective of crystal size distribution (Kah et al., 2022). The *Séítah* bedrock grain sizes strongly overlap the coarse-grained regolith grain sizes measured in both *Máaz* and *Séítah* targets (Figure 5) and the overlap of grain size persists when only SuperCam RMI measurements are considered (Figure S2a in Supporting Information S1). The only exceptions are rare outlier grains (9 across three *Máaz* targets) (Figure 5). We lack the resolution to establish if these outliers differ in some way other than size from other coarse-grained regolith grains (i.e., different chemistry or spectral character). Mixed regolith observations demonstrate that bedrock fragments grade into sizes that overlap the larger end of coarse-grained regolith grain sizes (Figures 1a, 2c and 4b). It is feasible that these outliers are misidentified bedrock fragments. Excluding these few outlier grains, the grain size overlap, combined with the mineralogical and chemical evidence of olivine, strengthens the link between the coarse-grained regolith and *Séítah* bedrock.

5.2.3. Grain Size Distributions in Máaz and Séítah

The range of coarse-grained regolith grain sizes is assessed to be roughly the same in both *Máaz* and *Séítah* (Figure 5), but the grain size distribution within each formation differs. A Shapiro-Wilk normality test revealed that the grain size measurements for each unit were not normally distributed and nonparametric methods were necessary. The grain size data ($N = 2,843$) were grouped by geologic unit (*Séítah*, *Máaz*) and a Wilcoxon rank-sum test, which assumes independence and an unknown distribution, evaluated the equality of medians between the groups. This test determined that the median grain size of coarse-grained regolith in the *Máaz* formation is statistically larger than the median grain size of coarse-grained regolith grains within the *Séítah* formation (1.4 mm (*Máaz*), 1.34 mm (*Séítah*)). The difference in median grain size might indicate a difference in the transport histories of coarse grains in *Máaz* and *Séítah*. However, the difference is comparable to the measurement variations observed between techniques (Section 5.2.1), such that future work would be required to establish the geologic significance and source of the difference.

5.2.4. Rounding

The sharpness of a grain's corners (referred to as angularity or roundedness) is a key parameter to texturally classify a grain and has been used as one indicator of grain abrasion and sorting processes (Krumbein & Sloss, 1963; Pettijohn et al., 1975; Tunwal et al., 2017). Sub-rounded and rounded grains dominate both *Máaz* and *Séítah* regolith targets (Figure 7), indicating the grains have undergone some degree of transport (e.g., Greeley et al., 2006; Kuenen, 1960; Sullivan & Kok, 2017). There does not appear to be a correlation between roundedness and *Máaz* versus *Séítah* setting (Figure 7). Targets with greater proportions of subangular and subrounded grains occur in both *Máaz* and *Séítah*, and targets with predominantly rounded grains occur in both formations. However, the smaller number of regolith targets evaluated for roundedness in *Séítah* might obscure the presence of a relationship (Figure 7).

There is no consistent trend between grain size and rounding in either *Máaz* or *Séítah* (Figure 17). For *Séítah*, statistically significant grain size differences between roundedness categories were not observed in either RMI or WATSON data (Figure 17, Figure S7 in Supporting Information S1). In RMI observations for *Máaz*, we observed that short-axis grain sizes increase in size with increasing roundedness. Grain size differences (determined by the short axis) are statistically observable between categories of roundedness (K-W, $p = 0.031$), with differences between the sub-angular and rounded classes (Wilcoxon, $p = 0.0035$) and the sub-angular and sub-rounded classes (Wilcoxon, $p = 0.039$). Neither the RMI data for long-axis grain size measurements nor the short- or long-axis data from WATSON show this same trend (Figure 17, Figure S7 in Supporting Information S1). The relationship between short-axis and rounding in RMI data from *Máaz* could indicate that some combination of

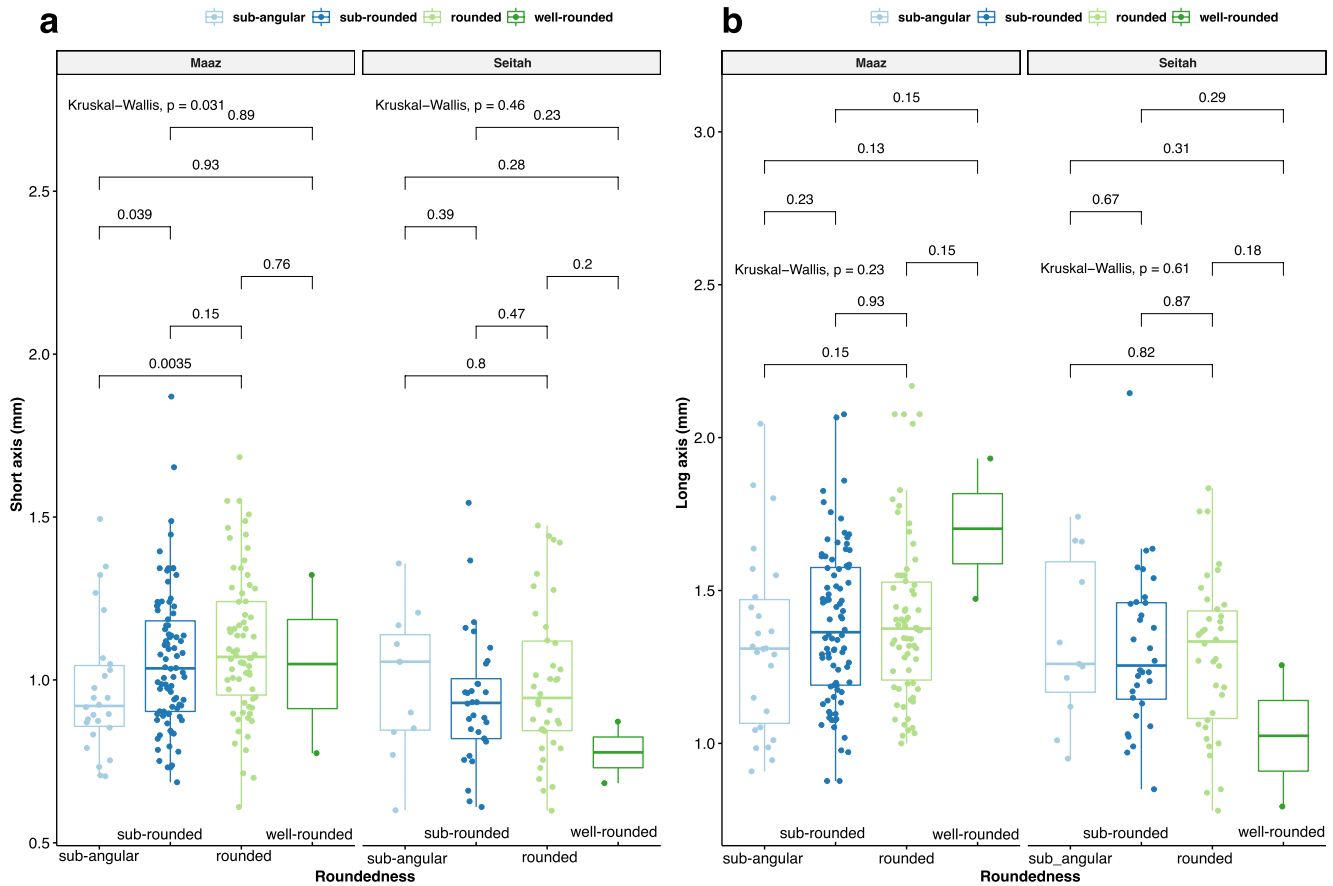


Figure 17. Short axis (a) and long axis (b) measurements for coarse regolith grains assessed for roundedness in the SuperCam Remote Micro Imager images. Roundedness classification-based boxplots are presented for the *Máaz* and *Séitah* targets within each panel. The p-values from the unit-based Kruskal-Wallis test and the subsequent Wilcoxon tests are presented, with $p < 0.05$ representing statistical significance. The equivalent diagram for Wide Angle Topographic Sensor for Operations and eNginering-only data is included in Figure S7 in Supporting Information S1.

factors such as transport distance, transport mechanism, and grain lithology yield larger grains within less angularity. More measurements would be required to investigate the robustness of this relationship.

5.3. Grain Size and Thermal Behavior

Regolith grain size is important for the thermal response of terrain. The thermal conductivity k of regolith, under Martian conditions, has been shown empirically to depend on atmospheric pressure and grain size, such that for a pressure of 613 Pa, $k = 0.00375 d^{0.467}$ where d is the grain size diameter in mm (Presley & Christensen, 1997). The thermal inertia (TI) of a material can be expressed with k as the thermal conductivity, r the bulk density and c the specific heat. Assuming a specific heat of $c = 850 \text{ J/kg/K}$ as that of basaltic rocks, then the thermal inertia will change mostly depending on the bulk density and, through k , on the regolith grain size. The bulk density of regolith granular material has been estimated to range between ~ 1 and 1.8 g/cm^3 , by via various spacecraft and surface interactions (e.g., Knuth et al., 2012; Moore et al., 1987; Morgan et al., 2018; Shaw et al., 2009; Sullivan et al., 2011). In particular, sand dunes have been estimated to have a bulk density of about 1.680 g/cm^3 (Edgett & Christensen, 1994). Grain size observations can therefore be used to provide estimates of the thermal inertia of the terrain, and conversely, thermal inertia observations can be used as a proxy for regolith grain sizes. In particular, for an intermediate value of density of 1.680 g/cm^3 and using the relationships described above, we estimate that the finer grain component ($< 500 \mu\text{m}$) should have TI values of less than 300 TIU, whereas the coarse regolith component of 1–2 mm size should have TI values of about 350–425 TIU. These estimates are in family with both orbital and in situ measurements of thermal inertia within the Crater Floor Campaign area. THEMIS values range between 200 and 450 TIUs, and MEDA sol-by-sol-derived values (up to Sol 320) range between 200 and 600 TI

units (Martinez et al., 2022a, 2022b). The orbital versus in situ differences are explained by the different spatial resolutions of the data sets.

Bramble et al. (2017) combined THEMIS studies of thermal inertia and grain size with CRISM spectral data in the NE Syrtis Major region to map different geomorphic units. The “Fractured Unit” surface consists of light-toned fractured blocks surrounded by dark-toned material and is rich in olivine, Mg-carbonate, and Fe/Mg-smectites. Low-lying areas are covered in aeolian material. These materials were interpreted to have a TI of 420.29 ± 20.74 corresponding to grains >1 mm, which is compatible with the olivine-rich coarse regolith grains described herein. Furthermore, this “Fractured Unit” mapped by Bramble et al. (2017) corresponds to the olivine-rich “Light Toned Floor” and “Mottled Terrain” units mapped by Goudge et al. (2015). The Light-Toned Floor unit of the Jezero Basin is the *Séítah* formation investigated by Perseverance, providing further support for a link between the olivine-rich coarse regolith grains and the olivine-rich *Séítah* bedrock. Future investigations can perform local regolith grain size studies at a single spot to calculate the grain size distribution with the actual-derived thermal inertia from MEDA and provide ground truth to these semi-empirical relationships that are generally used to calculate grain sizes.

5.4. Transportation and Origin

The fine-grained regolith type found on the Jezero crater floor has equivalents at each landing site explored in situ (e.g., Bell et al., 2000; Bridges & Ehlmann, 2017; Golombek et al., 2020; Herkenhoff et al., 2004; Lapotre & Rampe, 2018; Minitti et al., 2013; Soderblom et al., 2004; Sullivan et al., 2008). Regolith at these other sites whose grain sizes overlap with the fine-grained regolith type of this study are found in active dunes (Sullivan et al., 2008; Weitz et al., 2018), and in the interiors of inactive bedforms (Minitti et al., 2013; Weitz et al., 2006). Fine-grained regolith at other sites ranges from 50 to 800 μm depending on local setting (dune type, crest vs. trough of a bedform), but the median grain size of all targets falls between 100 and 150 μm (Herkenhoff et al., 2004; Sullivan et al., 2008; Weitz et al., 2006, 2018). The coarsest endmember of these grains is commonly found on ripple crests (Sullivan et al., 2008; Weitz et al., 2018). Major element chemistry of fine-grained regolith is broadly basaltic across landing sites (e.g., Arvidson et al., 2011; Gellert et al., 2006; O’Connell-Cooper et al., 2017, 2018; Yen et al., 2005), and variations are attributed to dust content, local inputs, or mineralogical sorting by grain size (Johnson et al., 2017; O’Connell-Cooper et al., 2018; Sullivan et al., 2008; Yen et al., 2008). Accordingly, the composition of fine-grained regolith in Jezero as determined by SuperCam LIBS data is similar to the fine-grained regolith composition at Gale (Cousin et al., 2022). Multispectral data support the overall basaltic nature of the fine-grained regolith across landing sites, but also reveal variations attributable to local input such as hematite at Meridiani, and the sulfur-rich soils at Gusev crater (Figure 18; Johnson et al., 2007; Wang et al., 2006). Collectively, the data across landing sites support that fine-grained regolith is a mixture of global dust and regional to local materials. The pyroxene-bearing nature of the Jezero fine-grained regolith links it to the pyroxene-bearing rocks of the crater floor (Figure 9a), but we cannot rule out larger, regional contributions to this pyroxene signature. It is reasonable to expect that there is olivine present in the fine-grained regolith, with *Séítah* as a source in proximity and a likely contributor to the coarse-grained regolith type. If olivine is present, however, it is not in sufficient quantities to influence the NIR slope of the fine-grained regolith spectra as it does that of the coarse-grained regolith spectra, nor is it indicated in the fine-grained LIBS regolith data (e.g., Figures 8–10, 18).

Bedforms armored with grains that fall in the size range of the coarse-grained regolith type of this study are widespread on Mars. These types of grains were observed armoring bedforms by rovers at Gusev, Meridiani, and Gale (Arvidson et al., 2011; Blake et al., 2013; Minitti et al., 2013; Soderblom et al., 2004; Yen et al., 2005). The sorting, roundedness, and spatial distribution of the coarse-grained regolith indicates that those grains are, or have been mobile. Their size and distribution suggest that these grains likely move by creep, meaning that finer, saltating grains impact these larger grains and move them across the surface (e.g., Sullivan & Kok, 2017). Over time, the wind will remove the finer grains, and concentrate these coarser grains. Varying composition of these grains across landing sites suggests a more local origin. Coarse grains observed on Gusev bedforms were interpreted to be Gusev plains basalt (Yen et al., 2005). Armoring grains (long axes 1–4.5 mm) in Meridiani were hematite-rich and clearly sourced from the local bedrock (e.g., Christensen et al., 2004; Weitz et al., 2006). Coarse grains armoring the Rocknest sand shadow at Gale crater had inputs from local bedrock, but also a lithology that was unidentified in the region around Rocknest (Meslin et al., 2013; Minitti et al., 2013). The Phase 2 Bagnold dune sands of Gale crater were interpreted to have incorporated nearby rock fragments based on an increased ferric

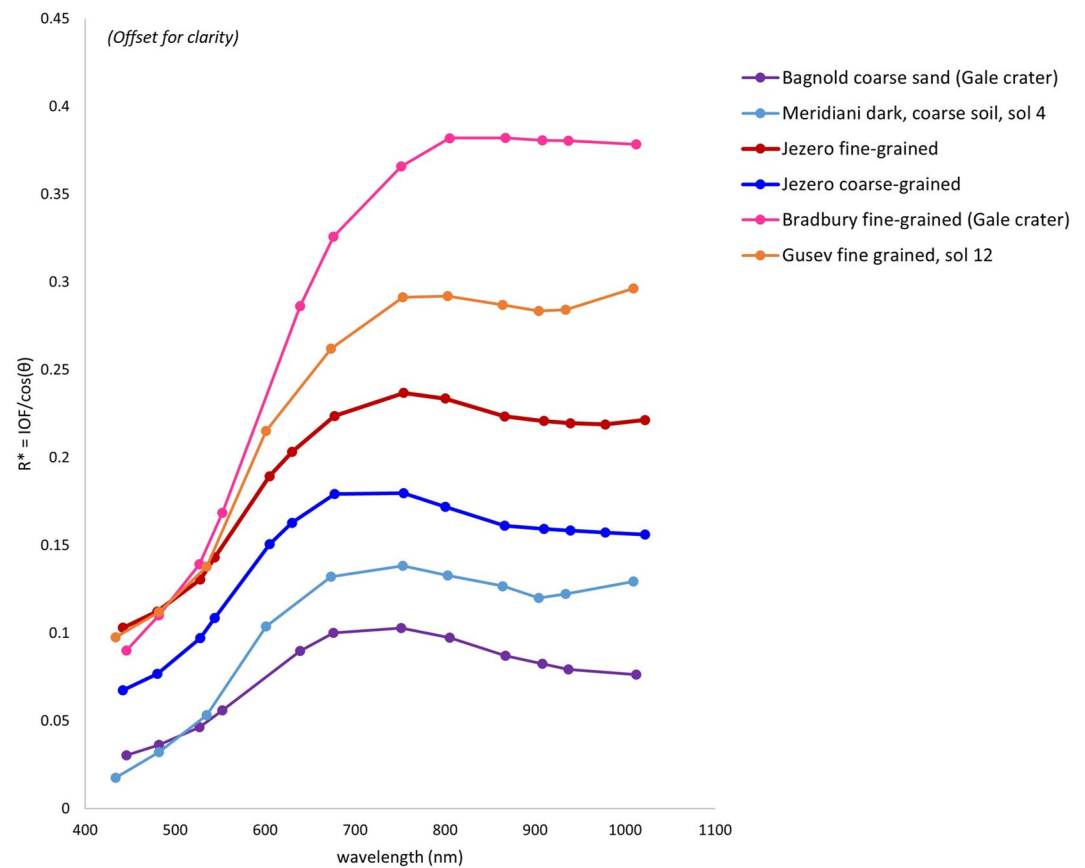


Figure 18. Regolith spectra from the Gusev crater and Meridiani Planum landing sites were collected by the Pancam instrument onboard the *Spirit* and *Opportunity* rovers (Bell et al., 2004a, 2004b). Gale crater spectra were collected by the Mastcam instrument onboard the *Curiosity* rover (Rice et al., 2022b).

iron component consistent with the surrounding hematite-bearing Murray formation (Johnson et al., 2018). The olivine composition and grain size of Jezero coarse-grained regolith overlap with grains measured within the olivine-rich *Séítah* formation, making that unit a likely source for these grains. A CRISM-derived parameter map of mafic components (orthopyroxene, clinopyroxene, and olivine; B. H. N. Horgan et al., 2020) within Jezero crater indicates an eastward deposition of olivine-rich material from the *Séítah* formation onto the neighboring *Máaz* formation. The spatial distribution of grain size averages indicates that targets with larger average grain sizes occur within and near *Séítah* (Figure 6). Those near *Séítah* but within *Máaz* occur near places where the scarp that defines most of the *Máaz-Séítah* boundary is muted or absent. Finding larger grains within *Séítah* and in these particular areas in *Máaz* is consistent with the model of transport of these grains from *Séítah* into *Máaz*. The larger average grain sizes suggest that the larger grains have, on average, made it less far from their source. As *Perseverance* has shown that the *Máaz* formation rocks do not contain olivine, the olivine signature observed must be coming from the olivine-rich coarse-grained regolith described herein. Paleowind directions interpreted from measurements of flute features on in-place rocks throughout the Crater Floor Campaign indicate winds from west to east, which could have transported olivine grains east from *Séítah* (Herkenhoff et al., 2023; Newman et al., 2022). A regional olivine-bearing unit is also present around Jezero crater (e.g., Kremer et al., 2019; Tarnas et al., 2021; Ruff & Hamilton, 2021). We cannot rule out the contribution from this unit to the coarse-grained regolith, but we expect that the proximity and similarity of the coarse-grained regolith of this study and the *Séítah* formation means that *Séítah* is an important contributor of olivine-bearing grains to the coarse-grained regolith.

The texture, chemistry, and mineralogy of rock fragments within mixed regolith are consistent with those of in-place rocks (Figures 1, 2, 9 and 10). This consistency supports the idea that mixed regolith rock fragments are products of weathering and erosion of local *Máaz* and *Séítah* rocks, or lag fragments from the erosion of overlying bedrock materials. In turn, this supports the hypothesis of Stack et al. (2020) that the *Us* surface is a lag deposit

of sediments from the breakdown of rocks and erosion of the landscape. Limited multispectral and imaging observations of an extensive *Us* unit deposit were obtained during the Perseverance traverse from the Crater Floor Campaign area to the delta. However, observations such as systematic Mastcam-Z clast surveys (post-drive Z34-Z110 images off rover starboard, e.g., Yingst et al., 2016) could permit further testing of this hypothesis.

5.5. Preparing for Regolith Sampling

The Perseverance sample handling system is equipped with a specialized bit to enable the regolith sample collection (Moeller et al., 2021), and the team intends to collect two regolith samples during the prime mission. The grain size, chemistry, and mineralogy measurements of this study support selection of sampling targets by placing the eventual sampling targets in the context of Jezero crater floor regolith characteristics. Future evaluation of potential collecting sites will include estimating the expected size distribution of the regolith grains to ensure that sufficient sample volumes are collected via the regolith sampling bit. Identifying a sampling target with a fine-grained regolith component like that characterized on the Jezero crater floor, including airfall dust, is of particular interest considering the potential of fine-grained regolith to provide regional to global insights (e.g., Grady et al., 2022; McLennan et al., 2012). Acquiring a regolith sample that includes contributions from more local components like the coarse-grained regolith type has the potential to extend understanding of the weathering and erosion histories of the units from which those components are derived. The type of investigation undertaken by this study can also be implemented during the exploration of Jezero crater beyond the crater floor, where regolith may have different characteristics because of different combinations of local, regional, and global inputs.

6. Conclusions

A multi-instrument study of the regolith at multiple scales in the Jezero crater floor units by the Perseverance rover identified three regolith components: fine-grained, coarse-grained, and mixed. Fine-grained regolith grains are <500 μm in size, generally redder in color, and comprise the underlying and matrix material for other regolith types and bedforms. Our analysis indicates that fine-grained regolith has a composition consistent with a mixture of minerals including ferric-oxides, pyroxene, and likely alteration products. While the mobility of this size fraction means that regional to global inputs are possible and likely, there is evidence to support the interpretation that the local pyroxene-rich rocks of the *Máaz* formation are contributing to the formation of fine-grained regolith in Jezero crater.

Coarse-grained regolith is found in aggregations around rocks, on top of bedrock slabs, and armoring bedforms. It is characterized by gray, 1–2 mm subrounded to rounded grains whose chemistry and mineralogy are dominated by olivine. Their grain size and composition overlap with olivine grains measured in the *Séítah* formation bedrock, making the *Séítah* formation a likely source for these grains. The population of coarse-grained regolith grains at Jezero that armor bedforms resemble armored bedforms observed at other landing sites. At all of these sites, the chemistry and mineralogy of coarse, armoring grains are strongly associated with the bedrock compositions of their respective landing sites, indicating that they are sourced locally. The presence of olivine-bearing coarse-grained regolith in both the *Séítah* and *Máaz* formations, where only *Séítah* bedrock is olivine-bearing, requires the transport of the coarse-grained regolith grains. The degree of rounding of the grains also indicates transport. Movement via creep caused by the impact of smaller, more mobile grains is the most likely mechanism of coarse-grained regolith transport.

Mixed regolith represents much of the Jezero crater floor surface traversed by Perseverance during the Crater Floor Campaign that is not covered by aeolian bedforms. It is characterized by fine-grained regolith as an unconsolidated-matrix or underlying material, scattered coarse olivine-rich grains, and larger rock fragments that share textural, chemical, and spectral properties with local *Máaz* and *Séítah* bedrock, depending on the unit under investigation. The similarity of rock fragments and local bedrock indicate the rock fragments are the products of weathering and erosion of local bedrock and/or lag materials from formerly overlying bedrock exposures.

The characterization of regolith by this work informs the collection of regolith samples by Perseverance, which will provide important insights into the weathering and alteration history of the Martian surface. A regolith sample that specifically incorporates the coarse-grained olivine-rich grains will provide a unique opportunity to compare those grains directly to the olivine-dominated *Séítah* formation core samples, ultimately answering questions regarding their source. Any alteration undergone by these grains in transport can be studied in detail

relative to olivine grains from the bedrock itself. It is possible that the coarse-grained component of regolith will change along Perseverance's traverse throughout the mission, and future regolith sampling efforts may not contain the olivine-rich grains. Even if the coarse-grained component of future regolith samples is not olivine-bearing, this study emphasizes the value of comparing any sampled coarse grains to the sampled local bedrock to understand the sources, transport histories and directions, and alteration pathways involved in the regolith formation. Similar avenues of investigation can be pursued between the fine-grained fraction of regolith and local rocks. Perhaps more importantly, the opportunity to collect fine-grained regolith at more than one location along the mission traverse can support a systematic evaluation of the global nature of this fraction. Finally, any regolith samples collected that are related to observed surface crusts will capture important chemistry that could inform the composition of the cementing material, and the role of atmospheric exchange in their formation.

Data Availability Statement

All image and spectrometer data presented here from the Mastcam-Z (Bell & Maki, 2021), WATSON (Beegle, 2021), and SuperCam (S. A. Maurice & Wiens, 2021) instruments are available through the GeoSciences Node of the PDS (<https://pds-geosciences.wustl.edu/missions/mars2020/>). All Mastcam-Z spectra and ROIs have been archived by Rice et al. (2023). The ImageJ software used for measuring grain size is available for free through the National Institute of Health. The software release and documentation can be found at <https://imagej.nih.gov/ij/index.html> (Rasband, 1997–2018). This research also made use of the *mar slab* software ecosystem (<https://zenodo.org/badge/latestdoi/498892781>) and the R software environment (<https://www.R-project.org/>) with R studio (<http://www.rstudio.com/>).

References

- Allen, C. C., Morris, R. V., Jager, K. M., Golden, D. C., Lindstrom, D. J., Lindstrom, M. M., & Lockwood, J. P. (1997). Martian regolith simulant JSC Mars-1. In *Paper presented at 28th Annual Lunar and Planetary Science Conference, Houston, TX*.
- Anderson, R. B., Forni, O., Cousin, A., Wiens, R. C., Clegg, S. M., Frydenvang, J., et al. (2022). Post-landing major element quantification using SuperCam laser induced breakdown spectroscopy. *Spectrochimica Acta, Part B: Atomic Spectroscopy*, 188, 106347. <https://doi.org/10.1016/j.sab.2021.106347>
- Arvidson, R. E., Ashley, J. W., Bell III, J. F., Chojnacki, M., Cohen, J., Economou, T. E., et al. (2011). Opportunity Mars Rover mission: Overview and selected results from Purgatory ripple to traverses to Endeavour crater. *Journal of Geophysical Research*, 11(E07), E00F15. <https://doi.org/10.1029/2010JE003746>
- Arvidson, R. E., DeGrosse, P., Jr., Grotzinger, J. P., Heverly, M. C., Shechet, J., Moreland, S. J., et al. (2017). Relating geologic units and mobility system kinematics contributing to Curiosity wheel damage at Gale Crater, Mars. *Journal of Terramechanics*, 73, 73–93. <https://doi.org/10.1016/j.jterra.2017.03.001>
- Arvidson, R. E., Guinness, E. A., Dale-Bannister, M. A., Adams, J., Smith, M., Christensen, P. R., & Singer, R. B. (1989). Nature and distribution of surficial deposits in Chryse Planitia and vicinity, Mars. *Journal of Geophysical Research*, 94(B2), 1573–1587. <https://doi.org/10.1029/JB094iB02p01573>
- Bayer, B. E. (1976). Color imaging array (U.S. Patent 3971065).
- Beegle, L. (2021). *Mars 2020 SHERLOC bundle*. NASA Planetary Data System. <https://doi.org/10.17189/1522643>
- Bell, J. F., & Maki, J. N. (2021). *Mars 2020 Mast Camera Zoom Bundle, from Arizona State University Mastcam-Z Instrument Team, calibrated products*. NASA Planetary Data System. <https://doi.org/10.17189/Q3TS-C749>
- Bell, J. F., III, Maki, J. N., Alwmark, S., Ehlmann, B. L., Fagents, S. A., Grotzinger, J. P., et al. (2022). Geological and meteorological imaging results from the Mars 2020 Perseverance rover in Jezero crater. *Science Advances*, 8(47), eabo4856. <https://doi.org/10.1126/sciadv.abo4856>
- Bell, J. F., III, Maki, J. N., Mehall, G. L., Ravine, M. A., Caplinger, M. A., Bailey, Z. J., et al. (2021). The Mars 2020 Rover Mast Camera Zoom (Mastcam-Z) multispectral, stereoscopic imaging investigation. *Space Science Reviews*, 217(1), 24. <https://doi.org/10.1007/s11214-020-00755-x>
- Bell, J. F., III, McSween, H. Y., Jr., Crisp, J. A., Morris, R. V., Murchie, S. L., Bridges, N. T., et al. (2000). Mineralogic and compositional properties of Martian soil and dust: Results from Mars Pathfinder. *Journal of Geophysical Research*, 105(E1), 1721–1755. <https://doi.org/10.1029/1999JE001060>
- Bell, J. F., III, Squyres, S. W., Arvidson, R. E., Arneson, H. M., Bass, D., Blaney, D., et al. (2004a). Pancam multispectral imaging results from the Spirit rover at Gusev Crater. *Science*, 305(5685), 800–806. <https://doi.org/10.1126/science.1100175>
- Bell, J. F., III, Squyres, S. W., Arvidson, R. E., Arneson, H. M., Bass, D., Calvin, W., et al. (2004b). Pancam multispectral imaging results from the opportunity rover at Meridiani Planum. *Science*, 306(5702), 1703–1709. <https://doi.org/10.1126/science.1105245>
- Berger, J. A., Schmidt, M. E., Gellert, R., Campbell, J. L., King, P. L., Flemming, R. L., et al. (2016). A global Mars dust composition refined by the Alpha-Particle X-ray Spectrometer in Gale Crater. *Geophysical Research Letters*, 43(1), 67–75. <https://doi.org/10.1002/2015GL066675>
- Beysac, O., Chide, B., Cousin, A., Clavé, E., Forni, O., Johnson, J. R., et al. (2021). Mafic chemistry and mineralogy (including olivine) of the coarse-grained regolith analyzed by SuperCam at Jezero Crater, Mars. *Paper presented at Annual Meeting of the American Geophysical Union, New Orleans, LA*.
- Bhartia, R., Beegle, L. W., DeFlores, L., Abbey, W., Hollis, J. R., Uckert, K., et al. (2021). Perseverance's scanning habitable environments with Raman and luminescence for organics and chemicals (SHERLOC) investigation. *Space Science Reviews*, 217(4), 58. <https://doi.org/10.1007/s11214-021-00812-z>
- Blake, D. F., Morris, R. V., Kocurek, G., Morrison, S. M., Downs, R. T., Ming, D. W., et al. (2013). Curiosity at Gale crater, Mars: Characterization and analysis of the Rocknest sand shadow. *Science*, 341(6153), 1239505. <https://doi.org/10.1126/science.1239505>

Acknowledgments

The authors would like to thank the Mars 2020 science and engineering teams for their work in the daily operations of the rover ensuring its safety and enabling the exploration of Jezero crater that has led to the collection of data presented here. The authors thank the regolith working group for helpful discussions and support of our work. Thanks to Alex Hayes, Kjartan Kinch, and Marco Merusi for their work in calibrating the Mastcam-Z image and multispectral data. The authors gratefully acknowledge all the instrument PULs and PDLs whose work to acquire, calibrate, process, and provide the highest quality instrument data enables scientific research. The authors would also like to thank the Arizona State University for funding a portion of this work. This research was supported by the NASA with contracts through the Jet Propulsion Laboratory to Ken Herkenhoff (80HQTR20T0096) and MEM (#1668585), and a portion of the research was carried out at the Jet Propulsion Laboratory, California Institute of Technology, under NASA contract 80NM0018D0004. Kjartan Kinch was supported by the Carlsberg Foundation Grant CF19-0023. M. Merusi received funding from the E.U.'s Horizon 2020 research and innovation program under the Marie Skłodowska-Curie Grant 801199. Any use of trade, firm, or product names is for descriptive purposes only and does not imply endorsement by the U.S. Government.

- Bramble, M. S., Mustard, J. F., & Salvatore, M. R. (2017). The geological history of Northeast Syrtis major, Mars. *Icarus*, 293, 66–93. <https://doi.org/10.1016/j.icarus.2017.03.030>
- Bridges, N., & Ehlmann, B. L. (2017). The Mars Science Laboratory (MSL) Bagnold Dunes Campaign, phase 1: Overview and introduction to the special issue. *Geophysical Research Letters*, 45(19), 3–19. <https://doi.org/10.1002/2017JE005401>
- Brown, A. J., Viviano, C. E., & Goudge, T. A. (2020). Olivine-carbonate mineralogy of the Jezero crater region. *Journal of Geophysical Research: Planets*, 125(3), e2019JE006011. <https://doi.org/10.1029/2019JE006011>
- Christensen, P. R., Wyatt, M. B., Glotch, T. D., Rogers, A. D., Anwar, S., Arvidson, R. E., et al. (2004). Mineralogy at Meridiani Planum from the Mini-TES experiment on the opportunity rover. *Science*, 306(5702), 1733–1739. <https://doi.org/10.1126/science.1104909>
- Clark, A. K., Weldon, R. J., Tuusaki, D. M., Schnabel, L., & Candelaria, M. P. (1982). Chemical composition of Martian fines. *Journal of Geophysical Research*, 87(B12), 10059–10067. <https://doi.org/10.1029/JB087iB12p10059>
- Cloutis, E. A., & Gaffey, M. J. (1991). Pyroxene spectroscopy revisited: Spectral-compositional correlations and relationship to geothermometry. *Journal of Geophysical Research*, 96, E5. <https://doi.org/10.1029/91JE02512>
- Cousin, A., Meslin, P. Y., Hausrath, E. M., Cardarelli, E., Lasue, J., Forni, O., et al. (2022). Soil diversity at Mars: Comparison of dataset from Gale and Jezero Craters. *Paper presented at 53rd Annual Lunar and Planetary Science Conference, The Woodlands, TX.*
- Curtis, S. A., Rice, M. S., Kraft, M. D., Mulcahy, S. R., Lapo, K. E., Dufflot, L. E., et al. (2022). Spectral variability in naturally weathered rock surfaces and implications for Mars. *Paper presented at 53rd Annual Lunar and Planetary Science Conference, The Woodlands, TX.*
- David, G., Meslin, P. Y., Dehouck, E., Gasnault, O., Cousin, A., Forni, O., et al. (2021). Laser-induced breakdown spectroscopy (LIBS) characterization of granular soils: Implications for ChemCam analyses at Gale crater, Mars. *Icarus*, 365(1), 114481. <https://doi.org/10.1016/j.icarus.2021.114481>
- Edgett, K. S., Caplinger, M. A., Maki, J. N., Ravine, M. A., Ghaemi, F. T., McNair, S., et al. (2015). Curiosity's robotic arm-mounted Mars Hand Lens Imager (MAHLI): Characterization and calibration status (MSL MAHLI Technical Report 0001; Version 2). <https://doi.org/10.13140/RG.2.1.3798.5447>
- Edgett, K. S., & Christensen, P. R. (1994). Mars aeolian sand: Regional variations among dark-hued crater floor features. *Journal of Geophysical Research*, 99(1), 1997–2018. <https://doi.org/10.1029/93JE03094>
- Edgett, K. S., Yingst, A. R., Ravine, M. A., Caplinger, M. A., Maki, J. N., Ghaemi, T. F., et al. (2012). Curiosity's Mars Hand Lens Imager (MAHLI) investigation. *Space Science Reviews*, 170(1–4), 259–317. <https://doi.org/10.1007/s11214-012-9910-4>
- Ehlmann, B. E., Edgett, K. S., Sutter, B., Achilles, C. N., Litvak, M. L., Lapotre, M. G. A., et al. (2017). Chemistry, mineralogy, and grain properties at Namib and high dunes, Bagnold dune field, Gale crater Mars: A synthesis of Curiosity rover observations. *Journal of Geophysical Research: Planets*, 122(12), 2510–2543. <https://doi.org/10.1002/2017JE005267>
- Ehlmann, B. L., Mustard, J. F., Murchie, S. L., Poulet, F., Bishop, J. L., Brown, A. J., et al. (2008). Orbital identification of carbonate-bearing rocks on Mars. *Science*, 322(5909), 1828–1832. <https://doi.org/10.1126/science.1164759>
- Farley, K., Stack, K. M., Horgan, B. H. N., Tarnas, J., Sun, V. Z., Shuster, D. L., et al. (2022). Aqueously altered igneous rocks on the floor of Jezero crater, Mars. *Science*, 377, 6614. <https://doi.org/10.1126/science.aba02196>
- Ferguson, R. L., Christensen, P. R., & Kieffer, H. H. (2006). High-resolution thermal inertia derived from the thermal emission imaging system (THEMIS): Thermal model and applications. *Journal of Geophysical Research*, 111(E12), E12004. <https://doi.org/10.1029/2006JE002735>
- Ferguson, R. L., Hare, T. M., Mayer, D. P., Galuszka, D. M., Redding, B. L., Smith, E. D., et al. (2020). Mars 2020 terrain relative Navigation Flight product generation: Digital terrain model and Orthorectified image mosaics. *Paper presented at 51st Lunar and Planetary Science Conference, The Woodlands, TX, Abstract #2020*. <https://doi.org/10.5066/P9QJDP48>
- Gellert, R., Rieder, R., Anderson, R. C., Brückner, J., Clark, B. C., Dreibus, G., et al. (2004). Chemistry of rocks and soils in Gusev crater from the Alpha Particle X-ray Spectrometer. *Science*, 305(5685), 829–832. <https://doi.org/10.1126/science.1099913>
- Gellert, R., Rieder, R., Brückner, J., Clark, B. C., Dreibus, G., Klingelhöfer, G., et al. (2006). Alpha Particle X-Ray Spectrometer (APXS): Results from Gusev crater and calibration report. *Journal of Geophysical Research*, 111(2), E02S05. <https://doi.org/10.1029/2005JE002555>
- Golombek, M., Warner, N. H., Grant, J. A., Hauber, E., Ansan, V., Weitz, C. M., et al. (2020). Geology of the InSight landing site on Mars. *Nature Communications*, 11(1), 1014. <https://doi.org/10.1038/s41467-020-14679-1>
- Goudge, T. A., Milliken, R. E., Head, J. W., Mustard, J. F., & Fassett, C. I. (2017). Sedimentological evidence for a deltaic origin of the western fan deposit in Jezero crater, Mars and implications for future exploration. *Earth and Planetary Science Letters*, 458, 357–365. <https://doi.org/10.1016/j.epsl.2016.10.056>
- Goudge, T. A., Mustard, J. F., Head, J. W., & Fassett, C. I. (2012). Constraints on the history of open-basin lakes on Mars from the composition and timing of volcanic resurfacing. *Journal of Geophysical Research*, 117, E00J21. <https://doi.org/10.1029/2012JE004115>
- Goudge, T. A., Mustard, J. F., Head, J. W., Fassett, C. I., & Wiseman, S. M. (2015). Assessing the mineralogy of the watershed and fan deposits of the Jezero crater paleolake system, Mars. *Journal of Geophysical Research: Planets*, 120(4), 775–808. <https://doi.org/10.1002/2014JE004782>
- Grady, M. M., Summons, R. E., Swindle, T. D., Westall, F., Kminek, G., Meyer, M. A., et al. (2022). The scientific importance of returning airfall dust as a part of Mars Sample Return (MSR). *Astrobiology*, 22(S1), S-176–S-185. <https://doi.org/10.1089/ast.2021.0111>
- Greeley, R., Arvidson, R. E., Bartlett, P. W., Blaney, D., Cabrol, N. A., Christensen, P. R., et al. (2006). Gusev crater: Wind-related features and processes observed by the Mars Exploration Rover Spirit. *Journal of Geophysical Research*, 111(E2), E02S09. <https://doi.org/10.1029/2005JE002491>
- Greeley, R., Leach, R., White, B., Iversen, J., & Pollack, J. B. (1980). Threshold windspeeds for sand on Mars: Wind tunnel simulations. *Geophysical Research Letters*, 7(2), 121–124. <https://doi.org/10.1029/GL007i002p00121>
- Hamilton, N. E., & Ferry, M. (2018). ggtern: Ternary diagrams using ggplot2. *Journal of Statistical Software, Code Snippets*, 87(3), 1–17. <https://doi.org/10.18637/jss.v087.c03>
- Hamilton, V. E., & Christensen, P. R. (2005). Evidence for extensive, olivine-rich bedrock on Mars. *Geology*, 33(6), 433–436. <https://doi.org/10.1130/G21258.1>
- Hayes, A. G., Corlies, P., Tate, C., Bell, J. F., III, Maki, J. N., Caplinger, M., et al. (2021). Pre-flight calibration of the Mars 2020 Rover Mastcam Zoom (Mastcam-Z) multispectral, stereoscopic imager. *Space Science Reviews*, 217(2), 29. <https://doi.org/10.1007/s11214-021-00795-x>
- Herkenhoff, K. E., Squyres, S. W., Arvidson, R. E., Bass, D. S., Bell, J. F., III, Bertelsen, P., et al. (2004). Evidence from Opportunity's microscopic imager for water on Meridiani Planum. *Science*, 306(5702), 1727–1730. <https://doi.org/10.1126/science.1105286>
- Herkenhoff, K. E., Sullivan, R., Newman, C., Paar, G., Baker, M., Viudez-Moreiras, D., et al. (2023). Comparison of ventifact orientations and recent wind direction indicators near the Mars 2020 Octavia E. Butler landing site on Mars. *Journal of Geophysical Research: Planets*, e2022JE007599. <https://doi.org/10.1029/2022JE007599>
- Hoefen, T. M., Clark, R. N., Bandfield, J. L., Smith, M. D., Pearl, J. C., & Christensen, P. R. (2003). Discovery of olivine in the Nili Fossae region of Mars. *Science*, 302(5645), 627–630. <https://doi.org/10.1126/science.1089647>

- Horgan, B., Rice, M., Garczynski, B., Johnson, J., Stack-Morgan, K., Vaughan, A., et al. (2022). Mineralogy, morphology, and geochronological significance of the Maaz formation and the Jezero Crater Floor. *Paper presented at 53rd Annual Lunar and Planetary Science Conference, The Woodlands, TX, Abstract #1680*.
- Horgan, B. H. N., Anderson, R. B., Dromart, G., Amador, E. S., & Rice, M. S. (2020). The mineral diversity of Jezero crater: Evidence for possible lacustrine carbonates on Mars. *Icarus*, 339(113526), 113526. <https://doi.org/10.1016/j.icarus.2019.113526>
- Iversen, J. D., & White, B. R. (1982). Saltation threshold on Earth, Mars and Venus. *Sedimentology*, 29(1), 111–119. <https://doi.org/10.1111/j.1365-3091.1982.tb01713.x>
- Johnson, J. R., Achilles, C., Bell, J. F., III, Bender, S., Cloutis, E., Ehlmann, B., et al. (2017). Visible/near-infrared spectral diversity from in situ observations of the Bagnold Dune Field sands in Gale Crater, Mars. *Journal of Geophysical Research: Planets*, 122(12), 2655–2684. <https://doi.org/10.1002/2016JE005187>
- Johnson, J. R., Bell, J. F., III, Bender, S., Cloutis, E., Ehlmann, B., Fraeman, A., et al. (2018). Bagnold Dunes campaign Phase 2: Visible/near-infrared reflectance spectroscopy of longitudinal ripple sands. *Geophysical Research Letters*, 45(18), 9480–9487. <https://doi.org/10.1029/2018GL079025>
- Johnson, J. R., Bell, J. F., III, Cloutis, E., Staid, M., Farrand, W. H., McCoy, T., et al. (2007). Mineralogic constraints on sulfur-rich soils from Pancam spectra at Gusev crater, Mars. *Geophysical Research Letters*, 34, L13202. <https://doi.org/10.1029/2007GL029894>
- Kah, L. C., Miniti, M., Cardarelli, E., Mangold, N., Liu, Y., Gupta, S., et al. (2022). Use of size frequency distributions in the interpretation of planetary surface materials. *Paper presented at 53rd Annual Lunar and Planetary Science Conference, The Woodlands, TX, Abstract #2044*.
- Khan, S., Stack, K. M., Yingst, R. A., & Bergmann, K. (2022). Characterization of clasts in the Glen Torridon region of Gale crater observed by the Mars Science Laboratory Curiosity Rover. *Journal of Geophysical Research: Planets*, 127(11), e2021JE007095. <https://doi.org/10.1029/2021JE007095>
- Kinch, K. M., Madsen, M. B., Bell, J. F., III, Maki, J. N., Bailey, Z., Hayes, A. G., et al. (2020). Radiometric calibration targets for the Mastcam-Z Camera on the Mars 2020 Rover mission. *Space Science Reviews*, 216(8), 141. <https://doi.org/10.1007/s11214-020-00774-8>
- Klima, R. L., Pieters, C. M., & Dyar, M. D. (2007). Spectroscopy of synthetic Mg-Fe pyroxenes I: Spin-allowed and spin-forbidden crystal field bands in the visible and near-infrared. *Meteoritics & Planetary Sciences*, 42(2), 235–253. <https://doi.org/10.1111/j.1945-5100.2007.tb00230.x>
- Knuth, M. A., Johnson, J. B., Hopkins, M. A., Sullivan, R. S., & Moore, J. M. (2012). Discrete element modeling of a Mars Exploration Rover wheel in granular material. *Journal of Terramechanics*, 49(1), 27–36. <https://doi.org/10.1016/j.jterra.2011.09.003>
- Kremer, C. H., Mustard, J. F., & Bramble, M. (2019). A widespread olivine-rich ash deposit on Mars. *Geology*, 47(7), 677–681. <https://doi.org/10.1130/G45563.1>
- Krumbein, W. C., & Sloss, L. L. (1963). *Stratigraphy and sedimentation* (p. 660). W. H. Freeman.
- Kuenen, P. H. (1960). SAND. *Scientific American*, 202(4), 94–113. <https://doi.org/10.1038/scientificamerican0460-94>
- Lapotre, M. G. A., Ehlmann, B. L., Minson, S. E., Arvidson, R. E., Ayoub, F., Fraeman, A. A., et al. (2017). Compositional variations in sands of the Bagnold Dunes, Gale Crater, Mars, from visible-shortwave infrared spectroscopy and comparison with ground truth from the Curiosity rover. *Journal of Geophysical Research: Planets*, 122(12), 2489–2509. <https://doi.org/10.1002/2016JE005133>
- Lapotre, M. G. A., & Rampe, E. B. (2018). Curiosity's investigation of the Bagnold dunes, Gale Crater: Overview of the two-phase scientific Campaign and introduction to the special collection. *Geophysical Research Letters*, 45(19), 10200–10210. <https://doi.org/10.1029/2018GL079032>
- Lemmon, M., Smith, M., Hueso, R., Munguira, A., Sanchez-Lavega, A., Viudez-Moreiras, D., et al. (2022a). Inside an active Martian storm in Jezero Crater. *Paper presented at 7th International Mars Atmospheric Modeling and Observations Workshop, Paris, France*.
- Lemmon, M., Smith, M. D., Viudez-Moreiras, D., de la Torre-Juarez, M., Vicente-Retortillo, A., Munguira, A., et al. (2022b). Dust, sand, and winds within and active Martian storm in Jezero Crater. *Geophysical Research Letters*, 49, 17. <https://doi.org/10.1029/2022GL100126>
- Liu, Y., Tice, M. M., Schmidt, M. E., Tremain, A. H., Kizovski, T. V., Hurowitz, J. A., et al. (2022). An olivine cumulate outcrop on the floor of Jezero crater, Mars. *Science*, 377, 6614–1519. <https://doi.org/10.1126/science.abe2756>
- Mandon, L., Quantin-Nataf, C., Royer, C., Beck, P., Fouchet, T., Johnson, J. R., et al. (2022a). Infrared reflectance of rocks and regolith at Jezero crater: One year of SuperCam observations. *Paper presented at 53rd Annual Lunar and Planetary Science Conference, The Woodlands, TX, Abstract #1631*.
- Mandon, L., Quantin-Nataf, C., Royer, C., Beck, P., Fouchet, T., Johnson, J. R., et al. (2022b). Reflectance of Jezero crater floor: 2. Mineralogical interpretation. *Journal of Geophysical Research: Planets*, e2022JE007450. <https://doi.org/10.1029/2022JE007450>
- Mangold, N., Gupta, S., Gasnault, O., Dromart, G., Tarnas, J. D., Sholes, S. F., et al. (2021). Evidence for a delta-lake system and ancient flood deposits at Jezero crater, Mars, from the Mars rover. *Science*, 374(6568), 711–717. <https://doi.org/10.1126/science.abc14051>
- Martinez, G. M., Sebastián, E., Vicente-Retortillo, A., Fischer, E., Toledo, D., Apéstitue, V., et al. (2022a). Thermal inertia and Albedo at Jezero crater as observed from the Mars 2020 MEDA instrument. *Paper presented at 53rd Annual Lunar and Planetary Science Conference, The Woodlands, TX*.
- Martinez, G. M., Sebastián, E., Vicente-Retortillo, A., Fischer, E., Toledo, D., Gómez, F., et al. (2022b). Thermal inertia and Albedo over the first 350 sols of the Mars 2020 mission. *Paper presented at 7th International Mars Atmospheric Modeling and Observations Workshop, Paris, France*.
- Maurice, S., Wiens, R. C., Bernardi, P., Caïs, P., Robinson, S., Nelson, T., et al. (2021). The SuperCam instrument suite on the Mars 2020 rover: Science objectives and mast-unit description. *Space Science Reviews*, 217(47), 47. <https://doi.org/10.1007/s11214-021-00807-w>
- Maurice, S. A., & Wiens, R. C. (2021). *Mars 2020 SuperCam Bundle*. NASA Planetary Data System. <https://doi.org/10.17189/1522646>
- McLennan, S. M., Sephton, M. A., Allen, C., Allwood, A. C., Barbieri, R., Betty, D. W., et al. (2012). Planning for Mars returned sample science: Final report of the MSR End-to-End International Science Analysis Group (E2E-iSAG). *Astrobiology*, 12(3). <https://doi.org/10.1089/ast.2011.0805>
- Merusi, M., Kinch, K. M., Madsen, M. B., Bell, J. F., Maki, J. M., Hayes, A. G., et al. (2022). The Mastcam-Z radiometric calibration targets on NASA's Perseverance rover: Derives irradiance time-series, dust deposition, and performance over the first 350 sols on Mars. *Earth and Space Science*, 9(12), e2022EA002552. <https://doi.org/10.1029/2022EA002552>
- Meslin, P.-Y., Gasnault, O., Forni, O., Schröder, S., Cousin, A., Berger, G., et al. (2013). Soil diversity and hydration as observed by ChemCam at Gale crater, Mars. *Science*, 341(6153), 1238670. <https://doi.org/10.1126/science.1238670>
- Million, C., St. Clair, M., & Rice, M. (2022). Software tools for rapid analysis of Mastcam-Z multispectral data. *Paper presented at 53rd Annual Lunar and Planetary Science Conference, The Woodlands, TX, Abstract #2533*.
- Miniti, M. E., Kah, L. C., Yingst, R. A., Edgett, K. S., Anderson, R. C., Beegle, L. W., et al. (2013). MAHLI at the Rocknest sand shadow: Science and science-enabling activities. *Journal of Geophysical Research: Planets*, 118(11), 2338–2360. <https://doi.org/10.1002/2013JE004426>

- Moeller, R. C., Jandura, L., Rosette, K., Robinson, M., Samuels, J., Silverman, M., et al. (2021). The Sampling and Caching Subsystem (SCS) for the scientific exploration of Jezero Crater by the Mars 2020 Perseverance rover. *Space Science Reviews*, 217(5), 5. <https://doi.org/10.1007/s11214-020-00783-7>
- Moore, H. J., Hutton, R. E., Clow, G. D., & Spitzer, C. R. (1987). Physical properties of the surface materials at the Viking landing sites on Mars (USGS Report 1389). <https://doi.org/10.3133/pp1389>
- Morgan, P., Grott, M., Knapmeyer-Endrun, B., Golombek, M., Delage, P., Lognonné, P., et al. (2018). A pre-landing assessment of regolith properties at the InSight landing site. *Space Science Reviews*, 214(104), 104. <https://doi.org/10.1007/s11214-018-0537-y>
- Murchie, S., Arvidson, R., Bedini, P., Beisser, K., Bibring, J.-P., Bishop, J. L., et al. (2007). Compact Reconnaissance Imaging Spectrometer for Mars (CRISM) on Mars Reconnaissance Orbiter (MRO). *Journal of Geophysical Research*, 112(E5), E05S03. <https://doi.org/10.1029/2006JE002682>
- Mustard, J. F., Ehlmann, B. L., Murchie, S. L., Poulet, F., Mangold, N., Head, J. W., et al. (2009). Composition, morphology, and stratigraphy of Noachian Crust around the Isidis basin. *Journal of Geophysical Research*, 114(7), E00D12. <https://doi.org/10.1029/2009JE003349>
- Mustard, J. F., Poulet, F., Gendrin, A., Bibring, J.-P., Langevin, Y., Gondet, B., et al. (2005). Olivine and pyroxene diversity in the crust of Mars. *Science*, 307(5715), 1594–1597. <https://doi.org/10.1126/science.1109098>
- Newman, C. E., Hueso, R., Lemmon, M. T., Munguira, A., Vicente-Retortillo, A., Apestigue, V., et al. (2022). The dynamic atmospheric and aeolian environment of Jezero crater, Mars. *Science Advances*, 8(21), eabn3783. <https://doi.org/10.1126/sciadv.abn3783>
- O'Connell-Cooper, C. D., Spray, J. G., Thompson, L. M., Gellert, R., Berger, J. A., Boyd, N. I., et al. (2017). APXS-derived chemistry of the Bagnold dune sands: Comparisons with Gale crater soils and the global Martian average. *Journal of Geophysical Research: Planets*, 122(12), 2623–2643. <https://doi.org/10.1002/2017JE005268>
- O'Connell-Cooper, C. D., Thompson, L. M., Spray, J. G., Berger, J. A., VanBommel, S. J., Gellert, R., et al. (2018). Chemical diversity of sands within the linear and barchan dunes of the Bagnold Dunes, Gale Crater, as revealed by APXS onboard Curiosity. *Geophysical Research Letters*, 45(18), 9460–9470. <https://doi.org/10.1029/2018GL079026>
- Pettijohn, F. J., Potter, P. E., & Siever, R. (1975). *Sand and sandstone* (pp. 81–82). Springer.
- Powers, M. C. (1953). A new roundness scale for sedimentary particles. *Journal of Sedimentary Petrology*, 23, 117–119. <https://doi.org/10.1306/D4269567-2B26-11D7-8648000102C1865D>
- Presley, M. A., & Christensen, P. R. (1997). The effect of bulk density and particle size sorting on the thermal conductivity of particulate materials under Martian atmospheric pressures. *Journal of Geophysical Research*, 102(4), 9221–9229. <https://doi.org/10.1029/97JE00271>
- Rasband, W. S. (1997–2018). ImageJ. National Institutes of Health. <https://imagej.nih.gov/ij>
- R Core Team. (2021). *R: A language and environment for statistical computing*. R Foundation for Statistical Computing. Retrieved from <https://www.R-project.org/>
- Rice, M. S., Johnson, J. R., Million, C. C., St. Clair, M., Horgan, B. N., Vaughan, A., et al. (2022a). Summary of Mastcam-Z visible to near infrared (VNIR) multispectral observations from Perseverance's mission in Jezero crater, Mars. *Paper presented at 53rd Annual Lunar and Planetary Science Conference, The Woodlands, TX, Abstract #2559*.
- Rice, M. S., Johnson, J. R., Million, C. C., St. Clair, M., Horgan, B. N., Vaughan, A., et al. (2023). Spectral variability of rocks and soils on the Jezero crater floor: A summary of multispectral observations from Perseverance's Mastcam-Z instrument. *Journal of Geophysical Research: Planets*, 128, e2022JE007548. <https://doi.org/10.1029/2022JE007548>
- Rice, M. S., Seeger, C., Bell, J., Calef, F., St. Clair, M., Eng, A., et al. (2022b). Spectral diversity of rocks and soils in Mastcam observations along the Curiosity rover's traverse in Gale crater, Mars. *Journal of Geophysical Research: Planets*, 127(8), e2021JE007134. <https://doi.org/10.1029/2021JE007134>
- Ruff, S. W. (2017). Investigating the floor of paleolake Jezero by way of Gusev crater. *Paper presented at Fourth Conference of Early Mars, Flagstaff, AZ, Abstract #3076*.
- Ruff, S. W., & Hamilton, V. E. (2021). A novel atmospheric removal technique for TES spectra applied to olivine and carbonate-rich bedrock in the Nili Fossae region, Mars. *Journal of Geophysical Research: Planets*, 126, 8. <https://doi.org/10.1029/2021JE006822>
- Salvatore, M. R., Goudge, T. A., Bramble, M. S., Edwards, C. S., Bandfield, J. L., Amador, E. S., et al. (2018). Bulk mineralogy of the NE Syrtis and Jezero crater regions of Mars derived through thermal infrared spectral analyses. *Icarus*, 301, 76–96. <https://doi.org/10.1016/j.icarus.2017.09.019>
- Scheller, E. L., Hollis, J. R., Cardarelli, E. L., Steele, A., Beegle, L. W., Bhartia, R., et al. (2022). Aqueous alteration processes and implications for organic geochemistry in Jezero crater, Mars. *Science*, 378(6624), 1105–1110. <https://doi.org/10.1126/science.aba5204>
- Schon, S. C., Head, J. W., & Fassett, C. I. (2012). An overfilled lacustrine system and progradational delta in Jezero crater, Mars: Implications for Noachian climate. *Planetary and Space Science*, 67(1), 28–45. <https://doi.org/10.1016/j.pss.2012.02.003>
- Shaw, A., Arvidson, R. E., Bonitz, R., Carsten, J., Keller, H. U., Lemmon, M. T., et al. (2009). Phoenix soil physical properties investigation. *Journal of Geophysical Research*, 114, E00E05. <https://doi.org/10.1029/2009JE003455>
- Soderblom, L. A., Anderson, R. C., Arvidson, R. E., Bell, J. F., III, Cabrol, N. A., Calvin, W., et al. (2004). Soils of Eagle crater and Meridiani Planum at the Opportunity rover landing site. *Science*, 306(5702), 1723–1726. <https://doi.org/10.1126/science.1105127>
- Stack, K. M., Williams, N. R., Calef, F., Sun, V. Z., Williford, K. H., Farley, K. A., et al. (2020). Photogeologic map of the Perseverance rover field site in Jezero crater constructed by the Mars 2020 Science Team. *Space Science Reviews*, 216(8), 127. <https://doi.org/10.1007/s11214-020-00739-x>
- St. Clair, M., Million, C., & Rice, M. (2022). marslab software suite. Retrieved from <https://zenodo.org/badge/latestdoi/498892781>
- Sullivan, R., Anderson, R., Biesiadecki, J., Bond, T., & Stewart, H. (2011). Cohesions, friction angles, and other physical properties of Martian regolith from Mars Exploration Rover wheel trenches and wheel scuffs. *Journal of Geophysical Research*, 116(E2), E02006. <https://doi.org/10.1029/2010JE003625>
- Sullivan, R., Arvidson, R., Bell, J. F., III, Gellert, R., Golombek, M., Greeley, R., et al. (2008). Wind-driven particle mobility on Mars: Insights from Mars exploration rover observations at “El Dorado” and surroundings at Gusev Crater. *Journal of Geophysical Research*, 113(E6), E06S07. <https://doi.org/10.1029/2008JE003101>
- Sullivan, R., & Kok, J. F. (2017). Aeolian saltation on Mars at low to moderate wind speeds. *Journal of Geophysical Research: Planets*, 122(10), 2111–2143. <https://doi.org/10.1002/2017JE005275>
- Sun, V. Z., Hand, K. P., Stack, K. M., Farley, K. A., Milkovich, S., Kronyak, R., et al. (2022). Exploring the Jezero crater 1230 floor: Overview of results from the Mars 2020 Perseverance rover's first science campaign. In *Paper presented at 53rd 1231 Annual Lunar and Planetary Science Conference, Houston, TX*.
- Swann, C., Sherman, D. J., & Ewing, R. C. (2020). Experimentally derived thresholds for windblown sand on Mars. *Geophysical Research Letters*, 47(3), e2019GL084484. <https://doi.org/10.1029/2019GL084484>

- Tarnas, J. D., Stack, K. M., Parente, M., Koeppel, A. H. D., Mustard, J. F., Moore, K. R., et al. (2021). Characteristics, origins, and biosignature preservation potential of carbonate-bearing rocks within and outside of Jezero crater. *Journal of Geophysical Research: Planets*, 126(11), e2021JE006898. <https://doi.org/10.1029/2021JE006898>
- Tornabene, L. L., Moersch, J. E., McSween, H. Y., Hamilton, V. E., Piatek, J. L., & Christensen, P. R. (2008). Surface and crater-exposed lithologic units of the Isidis Basin as mapped by coanalysis of THEMIS and TES derived data products. *Journal of Geophysical Research*, 113(E10), E10001. <https://doi.org/10.1029/2007JE002988>
- Tunwal, M., Mulchrone, K. F., & Meere, P. A. (2017). Quantitative characterization of grain shape: Implications for textural maturity analysis and discrimination between depositional environments. *Sedimentology*, 65(5), 1761–1776. <https://doi.org/10.1111/sed.12445>
- Viviano, C. E., Moersch, J. E., & McSween, H. Y. (2013). Implications for early hydrothermal environments on Mars through the spectral evidence for carbonation and chloritization reactions in the Nili Fossae region. *Journal of Geophysical Research: Planets*, 118(9), 1858–1872. <https://doi.org/10.1002/jgre.20141>
- Wang, A., Haskin, L. A., Squyres, S. W., Jolliff, B. L., Crumpler, L., Gellert, R., et al. (2006). Sulfate deposition in subsurface regolith in Gusev crater, Mars. *Journal of Geophysical Research*, 111, E2. <https://doi.org/10.1029/2005JE002513>
- Weitz, C. M., Anderson, R. C., Bell, J. F., III, Farrand, W. H., Herkenhoff, K. E., Johnson, J. R., et al. (2006). Soil grain analyses at Meridiani Planum, Mars. *Journal of Geophysical Research*, 111(E12), E12S04. <https://doi.org/10.1029/2005JE002541>
- Weitz, C. M., Sullivan, R. J., Lapotre, M. G. A., Rowland, S. K., Grant, J. A., Baker, M., & Yingst, R. A. (2018). Sand grain sizes and shapes in eolian bedforms at Gale crater, Mars. *Geophysical Research Letters*, 45(18), 9471–9479. <https://doi.org/10.1029/2018GL078972>
- Wentworth, C. K. (1922). A scale of grade and class terms for clastic sediments. *The Journal of Geology*, 30(5), 377–392. <https://doi.org/10.1086/622910>
- Wiens, R. C., Maurice, S., Robinson, S. H., Nelson, A. E., Cais, P., Bernardi, P., et al. (2021). The SuperCam instrument suite on the NASA Mars 2020 rover: Body unit and Combined system tests. *Space Science Reviews*, 217(1), 4. <https://doi.org/10.1007/s11214-020-00777-5>
- Wiens, R. C., Udry, A., Beyssac, O., Quantin-Nataf, C., Mangold, N., Cousin, A., et al. (2022). Compositionally and density stratified igneous terrain in Jezero crater, Mars. *Science Advances*, 8, 34. <https://doi.org/10.1126/sciadv.abo3399>
- Yen, A. S., Gellert, R., Schröder, C., Morris, R., Bell, J. F., III, Knudson, A., et al. (2005). An integrated view of the chemistry and mineralogy of Martian soils. *Nature*, 436(7047), 49–54. <https://doi.org/10.1038/nature03637>
- Yen, A. S., Morris, R. V., Clark, B. C., Gellert, R., Knudson, A. T., Squyres, S., et al. (2008). Hydrothermal processes at Gusev Crater: An evaluation of Paso Robles class soils. *Journal of Geophysical Research*, 113(E6), E06S10. <https://doi.org/10.1029/2007JE002978>
- Yingst, R. A., Cropper, K., Gupta, S., Kah, L. C., Williams, R. M. E., Blank, J., et al. (2016). Characteristics of pebble and cobble-sized clasts along the Curiosity rover traverse from Sol 100 to 750: Terrain types, potential sources, and transport mechanisms. *Icarus*, 280, 72–92. <https://doi.org/10.1016/j.icarus.2016.03.001>
- Yingst, R. A., Crumpler, L., Farrand, W. H., Li, R., Cabrol, N. A., & Neakrase, L. D. (2008). Morphology and texture of particles along the Spirit rover traverse from Sol 450 to Sol 745. *Journal of Geophysical Research*, 113, E12. <https://doi.org/10.1029/2008JE003179>